Master Thesis

Observational studies of the formation of coronal sigmoid in solar active regions

Takafumi Doi

Space Planetary Science Group

Department of Earth & Planetary Science

Graduate School of Science, The University of Tokyo

March, 2018

Abstract

The origin of solar flares has been identified as free magnetic energy accumulated in solar atmosphere. Sigmoid, which is a forward or inverse S-shaped bright feature appearing in soft X-ray, indicates sheared and twisted coronal magnetic structure (i.e. sheared arcade or magnetic flux rope) and likely to carry current and thus free magnetic energy. The formation processes of the magnetic structure have been shown as multiple magnetic reconnection events in the atmosphere (van Ballegooijen & martens 1989) as well as flux emergence (Fan 2001) from the convective zone. The former process produces a longer helical field line and a shorter submerging one. When the submerging loop passes the photospheric surface, magnetic cancellation on the PIL is observed (e.g., Martin 1985). The amount of the cancelled flux should be related to the internal flux of the sigmoidal magnetic structure.

In this thesis, I show the research about the relation between the formation of sigmoidal magnetic structure and the flux cancellation associated with magnetic reconnection in NOAA Active Region (AR) 11692, which is the bipolar active region and has only a polarity inversion line (PIL) and has little emerging flux. In two days prior to the formation of sigmoid in the AR, the coronal structure gradually evolves from a weakly sheared arcade to a J-shaped loop bundle, which is the southern part of the sigmoid.

I also estimated the accumulated flux in the J-shaped loop bundle after its formation. The position of footpoint of the J-shaped bundle is identified with the estimation of twist and dip shear angle, which is the signature of magnetic non-potentiality in the photospheric level. I assume that the footpoint exists in the region where the absolute value of twist shear angle is extremely high and the sign of twist shear angle can separate poloidal and axial components in the flux rope.

I extracted the cancelled flux coupled with each of the magnetic reconnection events related to sheared arcades, which is the inferred

origin of the J-shaped bundle, and derived their total cancelled flux as ~ 7.69×10^{18} Mx. I also estimated the total value of flux in the regions near the footpoint as 7.4 - 11 $\times$ 10^{19} Mx, which suggests that the cancelled flux is 7-10 % of the flux in the flux rope. The magnitude correlation of the two value is inverse compared with the previous researches. This reflects lower probability of the submergence of the reconnected short loop due to the long distance between its two footpoints.

要　旨

太陽大気中に蓄積された磁場の自由エネルギーは太陽フレアの起源として考えられてきている。軟 **X** 線で観測される **S** 字型あるいは逆 **S** 字型の明るい構造・シグモイドは、シアあるいはねじられたコロナ磁場構造(シアアーケード、磁気フラックスロープ)を表しており、電流やそれに伴う磁場の自由エネルギーを発生しやすい構造である。このようなシグモイド構造の形成過程として、対流層からの磁束管浮上 **(Fan 2001)** のほかに大気中での複数回の磁気リコネクションが考えられてきている **(van Ballegooijen & Martens 1989)**。磁気リコネクションによる形成過程では、長いヘリカルな磁力線と短い磁力線が形成される。このうちの短いものは下方へ沈み込み、光球表面を通過する際に、磁気中性線上での磁束相殺が観測される。**(**例 **Martin 1985).** 相殺された磁束の量は形成されたシグモイド磁場構造内部の磁束量に関連していると考えられる。

本学位論文では、双極磁場構造と単一の磁気中性線で構成され磁束の浮上の影響の少ない活動領域 **NOAA 11692** における、シグモイドの磁場構造の形成過程と大気中の磁気リコネクションに伴う光球での磁束相殺との関連性についての観測的研究を行った。この活動領域では、シグモイド構造が形成される **2** 日前以降において、シアの弱いアーケード型の磁束管がシグモイドを構成する南側の **J** 型形状へ変化していく過程が観測された。

まず **J** 型構造の光球における足元を特定するために、光球磁場の非ポテンシャル性をあらわすパラメター、すなわち観測磁場から推定されるポテンシャル磁場と観測磁場との角度差**(dip shear angle** および **twist shear angle)**を黒点半暗部において導出した。これらが特異な値をとる領域を **J** 型構造の足元であると推定した。また、正・負に高い **twist shear angle** をとる領域を形成された **J** 型フラックスロープ内部のそれぞれ軸方向成分・軸と垂直方向成分の磁束であるとした。

J 型構造の形成に関わる磁気リコネクションによるコロナ中の増光、および対応する磁束相殺を抽出した。相殺された磁束の総計は $\mathbf{7.69 \times 10^{18}}$ **Mx** である。一方で、形成後の **J** 型構造内部の磁束量を推

定した。この領域における磁束の総和は **7.4 - 11** $\times$ **10^{19} Mx** である。すなわち、相殺された磁束はフラックスロープ内の磁束の **7 – 10 %** である。これら **2** つの値の大小関係は、先行研究のものと逆であり、これは活動領域 **NOAA 11692** における正・負の磁気要素間が長いために、リコネクション後の短い磁気ループが光球下に沈みこむことができなくなることを示唆している。

Contents

1.Introduction

1.1 Solar flares and pre-eruptive configurations

Solar flares are explosive phenomena observed in the solar atmosphere. They have been thought as energy releases in the form of kinetic and thermal energies, and strongly enhanced electromagnetic radiation over a wide range of wavelength, from radio wave to γ-ray. The radiative increase is relatively significant in the extreme ultraviolet (EUV) and soft X-ray, whose main origins are flare ribbons in the chromosphere and post-flare loops in the corona. The formation of flare ribbons and post-flare loops has been explained for a long time in the two-dimensional standard CSHKP model (Carmichael 1964; Hirayama. 1973; Kopp & Pneumann 1976; Sturrock & Coppi 1966) based on several cartoons. *Yohkoh* satellite observed solar flares in soft X-ray and enclosed that there are a small island-like feature (plasmoid) moving upward and a cusp-shaped bright feature appearing after the onset of flare (**Figure 1.1 (a)**). Based on observations of the *Yohkoh* satellite, the two-dimensional CSHKP model was revised to the three-dimensional picture (**Figure 1.1 (b)**, Shibata et al. 1995). In the model, a pre-eruptive configuration is initially constrained by the background magnetic fields. The eruption of the pre-eruptive configuration stretches the background fields and forms a magnetic dissipation region, which is called a current sheet (CS), between their two legs. If the CS becomes thinner than a threshold, magnetic reconnection occurs (Lin & Forbes 2000). The magnetic reconnection forms a post-flare loops, whose shape is like an arcade. Flare ribbons originate from heating by energy transport from the magnetic reconnection site. On the other hand, the reconnection releases energy upward that induces rapidly, enhances radiation, and frequently associates with a coronal mass ejection (CME).

The pre-eruptive configuration has been modelled to be a helical magnetic flux rope (MFR, left panel of **Figure 1.2**, Shibata et al. 1995; Titov & Démoulin 1999; Vourlidas et al. 2013) or a sheared arcade (right panel of **Figure 1.2**, Antiochos et al. 1999; Sturrock & Coppi 1966). An MFR is defined as a coherently helical magnetic structure with all field lines wrapping around the central axis at least one turn.

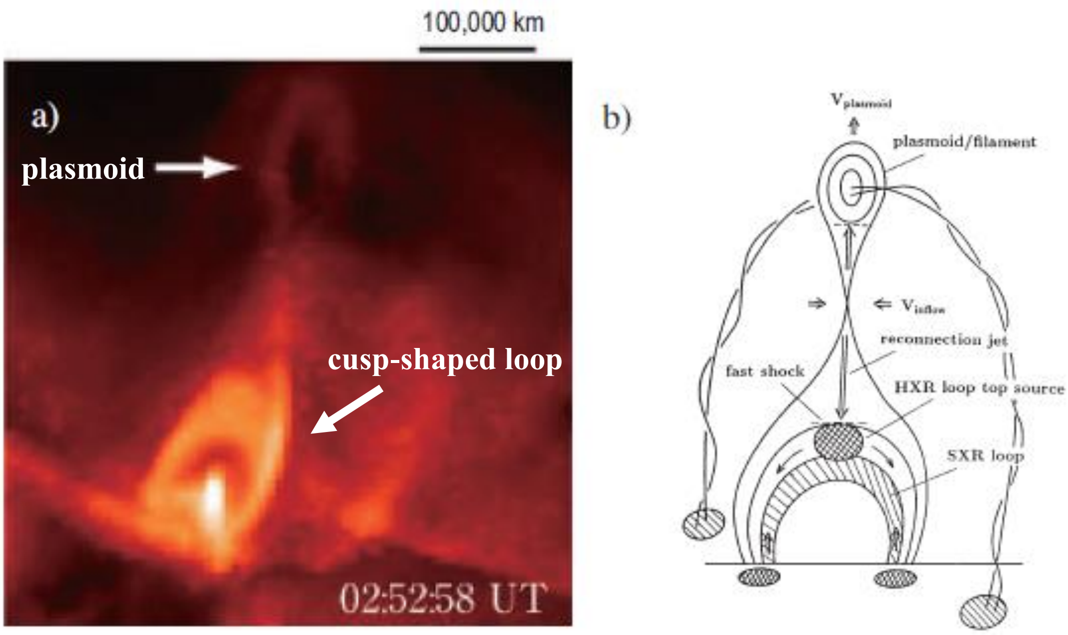

Figure 1.1 (a) Soft X-ray image of a long-durational-event (LDE) flare observed by the *Yohkoh* satellite (from Shibata & Magara 2011). (b) Schematic picture of a modified version of the CSHKP model, incorporating the new features discovered by the *Yohkoh* satellite (Shibata et al. 1995) .

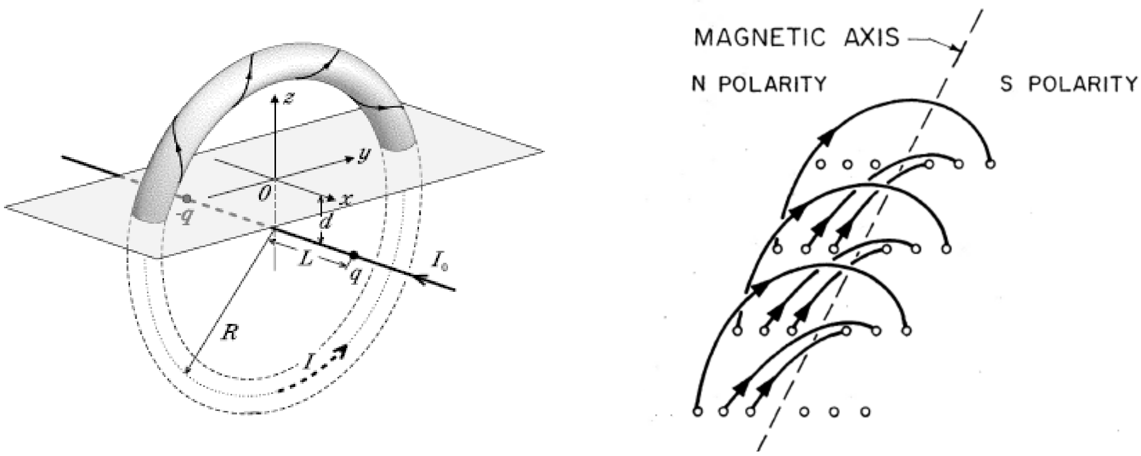

Figure 1.2 Schematic images of magnetic structures in a flux rope (left panel, from Titov & Démoulin 1999) and a sheared arcade (right panel, from Sturrock & Coppi 1966).

1.2 Manifestation of the pre-eruptive configurations

A forward or inverse S-shaped bright feature appearing in soft X-ray (e.g. **Figure 1.3** from Mckenzie & Canfield 2008) was named a sigmoid (Rust & Kumar 1996). Sigmoids have been discovered and researched since the *Yohkoh* mission. Sigmoids have been found to be important pre-eruptive coronal signatures (Gibson et al. 2002; Hudson et al. 1998; Rust & Kumar 1996; Sterling & Hudson 1997).

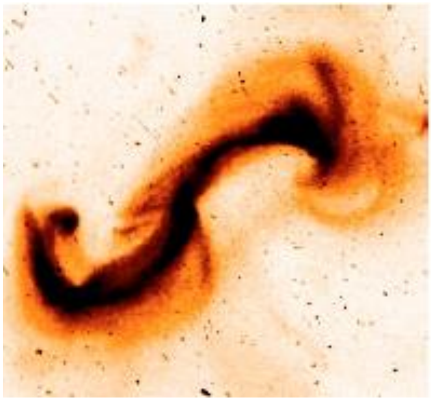

Figure 1.3
Hinode/XRT image of coronal sigmoid prior to an eruption (from Mckenzie & Canfield 2008).

A statistical study found sigmoidal active regions more likely to be eruptive (Canfield et al. 1999). This correlation should be acceptable, since non-potential, i.e., twisted or sheared, magnetic field lines produce S-shaped currents thus free magnetic energy, which is the surplus magnetic energy compared with the energy of potential magnetic field, satisfying $\boldsymbol{\nabla} \times \boldsymbol{B} = \boldsymbol{0}$, in the corona. The sigmoidal emission pattern is expected to be due to the dissipation of free magnetic energy in a CS at the interface between the helical magnetic flux rope and the ambient field (Gibson et al. 2006; Kliem et al. 2004). Green et al. (2007) showed that the existence of the twisted field lines in sigmoids is supported by the conversion of twist, which is the number of windings of the field lines around the flux rope axis per a unit length, into writhe, which is the number of windings of the flux rope axis per a unit length, under the assumption of helicity conservation.

The sigmoidal emission pattern does not mean the existence of continuous sigmoidal field lines. Mckenzie & Canfield (2008) described a long-lasting (about 2 days) sigmoid that consisted of two J-shaped bundles of loops. The straight sections of the Js lay in anti-parallel to each other on opposite sides of a polarity inversion line. Although previous studies revealed that CME-productive active regions often show sigmoidal shapes in the EUV and/or soft X-ray images prior to the eruption, it does not mean that the corresponding magnetic field lines must be highly twisted. Alternatively, they could consist of two groups of sheared arcades, making up a sigmoidal shape apparently (Cheng & Ding 2016; Kliem et al. 2004; Schmieder et al. 2015; Titov & Démoulin 1999).

1.3 The formation of sigmoids or filaments

It has been shown that the formation mechanism of sigmoid has two possibilities; flux emergence and flux cancellation.

1.3.1 Flux emergence

Flux emergence model is that an MFR in the convection zone emerges into the corona by buoyancy as a coherent structure (Fan 2001; Gibson et al. 2004). **Figure 1.4** shows the magnetic structure resulted from an emerged twisted flux tube (from Gibson et al. 2004). There are shown to be separatrix surfaces (purple lines), where the linkage of magnetic field lines changes drastically, and dipped structure (black lines) that material can be collected and observed as a Hα filament. By the flux emergence, opposite J-shaped loops and S-shaped loops exist simultaneously, which is observed as sigmoid (Archontis et al. 2009). Some observational studies also stand for the emergence of the MFR from below the photosphere to the corona (Lites 2005; Okamoto et al. 2008, 2009). δ type sunspots, in which two umbrae with opposite magnetic polarities are embedded in one penumbra, may be produced by the emergence of a twisted MFR (Ishii et al. 1998; Kurokawa et al. 2002). Poisson et al. (2013) suggested that the δ-spot could be due to the emergence of a deformed single tube that has a downward convex structure at its middle part with kinking.

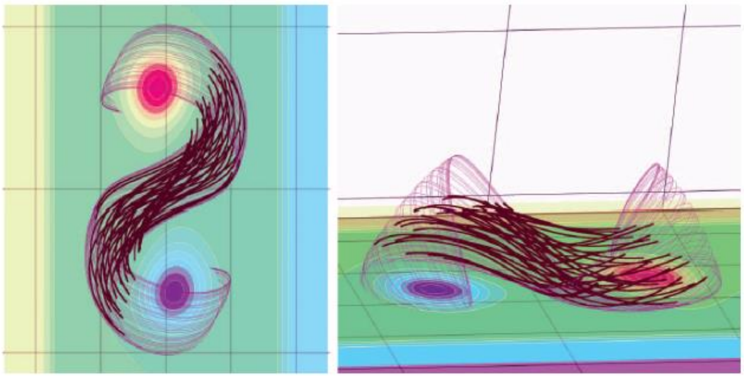

Figure 1.4 Simulation using flux emergence model. The purple lines show separatrix surfaces and the black lines show the dipped structure (from Gibson et al 2004).

1.3.2 Flux cancellation

Sigmoidal structure can be also formed with multiple numbers of magnetic reconnection in the atmosphere above the photosphere. The first numerical study of the model sets a bipolar region where the converging motion toward the polarity inversion line (PIL), which is the boundary between regions of positive and negative magnetic field, and the shearing motion along the PIL occur (van Ballegooijen & Martens 1989). These motions lead to the magnetic reconnection in the atmosphere, producing a shorter loop that submerges. When the submerging loop passes the photospheric surface, positive and negative magnetic elements look colliding each other and vanishing on the PIL, which is the magnetic cancellation. Thus, the magnetic flux measured at the photosphere at the PIL shows a decrease as a function of time (Martin et al. 1985). At the same time, a longer loop is produced by the reconnection to connect the magnetic polarities located in a distance, forming a sheared structure along the PIL, as shown in **Figure 1.5** (d to f).

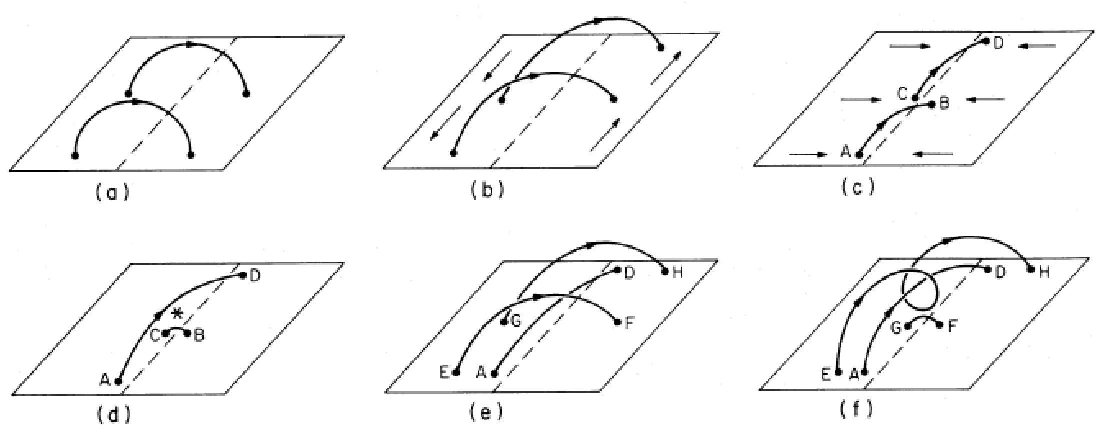

Figure 1.5 Flux cancellation in a bipolar region (from van Ballegooijen & Martens 1989). The rectangle represents the photospheric surface. The dashed line is the PIL. (a) Initial potential field. (b) sheared field lines by flows along the PIL. (c) sheared field lines converge toward the PIL to enlarge magnetic shear. (d) magnetic reconnection produces a longer loop AD and a shorter loop CB which submerges. (e) overlying loops EF and GH pushed to the PIL. (f) reconnection produces a helical loop EH and a shorter loop GF which submerges.

Some observational studies have shown the evidence that sigmoidal structure is formed by the reconnection occurring above the photosphere. An analysis of the temperature structure of a sigmoid shows that the plasma in the J-shaped arcades has a higher temperature than that in the S-shaped flux if both are simultaneously visible (Tripathi et al. 2009). They argued that the J-shaped arcades are likely reconnecting to the S-shaped flux, thus having a higher temperature but starting to cool down after leaving the reconnection site. Coronal plasma near the axis of the inferred flux rope is cooler than the double-J shaped sigmoid at its edge. Cheng et al. (2014) studied the formation of the hot channel-like MFR observationally. Through analyzing the long-term evolution of an evolving sigmoidal active region, they found that the twisted field, indicated by continuous sigmoidal hot threads, is formed via the reconnection of two groups of sheared arcades near the PIL a half day before the eruption. The temperature of the twisted field and sheared arcades, derived by the differential emission measure (DEM) technique, is higher than that of the ambient volume, indicating that the reconnection takes place and heats the plasma therein. They also confirmed that the reconnection is driven by the shearing and converging motions near the PIL at the photosphere. The MFR can even be formed in the lower atmosphere (e.g., Wang et al. 2015), via, for example, a series of magnetic reconnection in the chromosphere, and sometimes be heated up to the coronal temperature as visible in the hot coronal images (131 and 94 Å) from AIA onboard *SDO* satellite (Kumar et al. 2015, 2017; Li & Zhang 2015).

Green et al. (2011) and Green & Kliem (2009) showed observations supporting that series of the reconnection in sheared arcades are driven by the flux convergence and subsequent cancellation at the photosphere, forming a sigmoid in the corona. This process of photospheric magnetic evolution can provide an observational method to investigate the flux content of the flux rope, because the flux of a submerging field line should be related to the flux of helical field lines newly produced in the corona. However, they suggested that the amount of the cancelled flux at the photosphere is unlikely to be equal to the amount of flux being built into the flux rope. As discussed in Green et al. (2011), the exact flux content depends on the level of shear in the arcade and on the length of the PIL that experiences reconnection events, shown in **Figure 1.6**, which is the elaborated cartoon of **Figure 1.5**. Moreover, the necessary converging motions at the PIL can be easily supplied by super-granular flows in the photosphere, which makes the flux cancellation episodes a natural part of the long-term evolution of ARs, although the flux cancellation generally occurs at discrete locations along the PIL. Application of magnetic cancellation to the formed rope flux therefore needs coupling of each reconnection event in the atmosphere with each cancellation.

Several studies have already derived the time scale in the formation of an MFR via series of magnetic reconnection and the amount of cancelled magnetic flux observed at the photosphere (Baker et al. 2012; Green et al. 2011; Martin et al. 1985; Sterling et al. 2010). They showed that it takes a few days to form an MFR in the former bipolar region. They estimated the amount of the cancelled flux in the PIL by observationally measuring the amount of vanished flux in the long period.

Savcheva et al. (2012) reported that 60-70 % of the cancelled flux exists in the magnetic flux in the flux rope. In that study, they quantified the cancelled flux by using the time evolution of the line-of-sight magnetogram with Michelson Doppler Imager onboard *Solar and Heliospheric Observatory*. They also quantified the magnetic flux in the flux ropes with the extrapolation of non-linear force free field (NLFFF) modeling.

The method of NLFFF extrapolation is the flux insertion method, described in van Ballegooijen (2004).

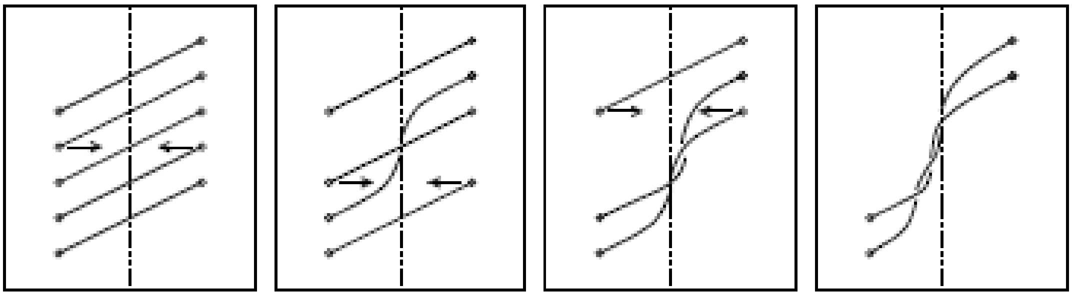

Figure 1.6 Schematic images of a cancellation episode which consists of three cancellation events and transforms the part of the initial arcade shown in the first panel into a flux rope. The PIL is drawn dashed. The ratio of footpoint displacement of the sheared arcade loops to the length of the active section of the PIL (where cancellation proceeds) is 2:3. Correspondingly, 2/5 of the flux is transformed into the rope, while 3/5 cancelled (Green et al. 2011).

1.4 Purpose of this thesis

The ratio of the cancelled flux to the sigmoidal flux can be important value to express the evolution of sigmoid associated with flux cancellation process. To estimate the ratio, the additional condition necessary to think should be where each magnetic reconnection event occurred in the atmosphere. Each coronal reconnection event should be linked to each flux cancellation observed at the photosphere, so that we could understand how series of reconnection in the corona make changes in magnetic field configuration and finally lead to a sigmoid, i.e., an MFR.

In this study, to couple each reconnection event with each cancellation event, I need the information of either the time difference between when magnetic reconnection occurred and when the flux cancellation at the PIL occurred, or where the PIL is. The sigmoid formation can be also contributed by the emergence of twisted flux tube, which results in forming δ-spot in the photospheric surface. Therefore, in order to explore the pure effect of magnetic reconnection to sigmoid formation, one approach should be a data analysis of bipolar active regions (β-type sunspots), where the number of sunspots is small and we can easily identify how magnetic structure evolves and little contribution from flux emergence exists.

Additionally, in order to estimate the internal flux of the flux rope, I introduce the magnetic parameters "shear angles," which is defined in the following section (**Section 3**), to the estimation and the qualitative extrapolation of magnetic configuration.

This thesis consists of the following sections. In **Section 2**, the observational instruments and the process of data selection are described. In **Section 3**, I described some details of data analysis and methods used in my study. In **Section 4**, the results from the data analyses are described. In **Section 5**, I discuss the results. In **Section 6**, the conclusion and the summary are shown.

2. Observations and data selection

2.1 Instrument description

In this study, I analyzed observational data from two satellites: *Hinode* satellite (Kosugi et al. 2007) and *Solar Dynamics Observatory* (*SDO*, Chamberlin et al. 2012), whose images are shown in **Figure 2.1** below.

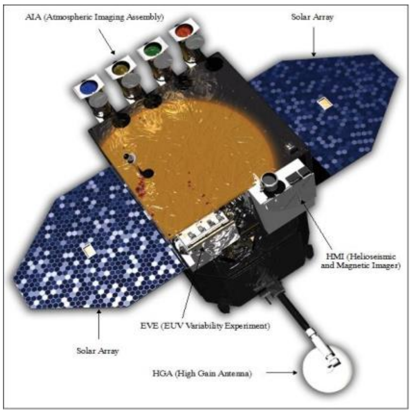

Figure 2.1. Artificial images of *Hinode* satellite (left) and *SDO* (right).

2.1.1 Imaging of coronal magnetic structures

The coronal magnetic field can be imaged in soft X-ray or EUV wavelength as the loop-like structure. In this study, I used soft X-ray images of active regions (384 x 384 pixels) acquired by the X-ray Telescope (XRT, Golub et al. 2007; Kano et al. 2008) onboard *Hinode*, whose spatial resolution is 1.03" / pixel, and EUV full-disk images (4k x 4k pixels) acquired by Atmospheric Imaging Assembly (AIA, Lemen et al. 2012) onboard *SDO*, whose spatial resolution is 0.6" / pixel. XRT is a grazing incident telescope with CCD detector. It has two filter wheels that insert one or two filters in the optical path. The filters include X-ray analysis filters for selecting a wavelength band in a soft X-ray (1 – 200 Å) and G-band (4305 Å) filter for photospheric images. Of the X-ray filters, thin Be filter (Be_thin) is the best suitable to identify high temperature (> 1 MK) component in coronal structures. The frequency of exposures is variable, controlled by observing table, which can be changed by observers, depending on the target of observations. XRT multiple filters and we can identify the high-temperature loop structures most clearly in Be_thin filter. The AIA is the suit of four normal incident telescopes, each of which has segmented primary/secondary mirrors with a different multilayer coating each, providing images taken at a variety of wavelengths in EUV and ultraviolet (UV). AIA images are acquired at a cadence of 12 seconds in seven EUV channels and 24 seconds in two UV ones. This study uses 131 Å (Fe VIII, Fe XXI, Fe XXIII, $T \sim$ 0.4, 10, 16 MK) and 171 Å (Fe IX, $T \sim$ 0.7MK) for the identification of coronal hot and cool loops. Also, 304 Å (He II, $T \sim$ 0.05 MK) and 1600 Å (C IV and continuum, $T \sim$ 0.1 MK and 5000 K) images were used for identifying the location of the chromospheric filament threads and flare ribbons near the PIL. These structures are useful as fiducial marks for co-aligning with images from other instruments.

2.1.2 Measurements of magnetic fields at the photosphere

Magnetic field at the photosphere can be measured with Heliospheric and Magnetic Imager (HMI, Schou et al. 2012) onboard *SDO* and Solar Optical Telescope / Spectropolarimeter (SOT/SP, Lites et al. 2007; Shimizu et al. 2008; Suematsu et al. 2008; Tsuneta et al. 2008) onboard *Hinode*. I used magnetic field vector data processed by both of them in this study.

In both of SOT/SP and HMI instruments, the measurement methods of magnetic field use the involved physical processes on the Zeeman effect, which is the effect of splitting a spectral line into several components in the presence of a magnetic field and associated polarization of light and results in observed Stokes profiles *IQUV*. The Stokes profile *I* represents the total light intensity. The Stokes profiles *Q* and *U* represent the linear polarization of light in the direction of 45 and -45 degrees. The Stokes profile *V* represents the circular polarization. The HMI instrument measures the Stokes profiles at six points in the Fe I 6173.3 Å absorption line (Schou et al. 2012). The HMI Stokes *I*, *Q*, *U*, and *V* data are inverted within the bounding box by using the Very Fast Inversion of the Stokes Vector (VFISV) code, which assumes a Milne-Eddington (ME) model of the solar atmosphere, to yield the vector magnetogram. Space-weather HMI Active Region Patches (SHARP) with HMI data is vector magnetic field data focusing on a box containing an active region. HMI SHARP data is acquired at a cadence of 12 seconds and at a spatial resolution of 0.5" / pixel.

SOT/SP also acquires vector magnetic field data (level2 data) but uses Fe I 6302.5 and 6301.5 Å absorption lines and nearby continuum (Lites et al. 2007). SOT/SP acquires line profiles by using a narrow slit of 0.16 × 151 arcsec. Spectra of the two lines are simultaneously taken in orthogonal linear polarizations, whose combined data reduces spurious polarization from any residual image jitter or solar evolution. In the SOT/SP, the spectro-polarimetric maps of active regions are made by scanning the narrow slit of north-south direction in the east-west direction across a field of view (FOV). SOT/SP has several modes of operation, two of which are normal map mode and fast map mode. The normal map mode produces polarimetric accuracy of 0.1 % with 0.15 × 0.16 arcsec per a pixel. It takes 83 minutes to scan a 160-arcsec-wide area, which is enough to cover a moderate-sized active region. As for the fast map mode, by reducing the scanning size, the cadence becomes faster (~30 minutes cadence for a 160 arcsec scan with a spatial resolution of 0.30 and 0.32 arcsec pixel in the east-west and the north-south direction respectively). The fast map mode summed the Stokes profiles at two slit positions with each integration time of 1.6 second and with two pixels along the slit, which makes the polarization accuracy a factor of 1.15 better than the normal map mode does (Tsuneta et al. 2008).

In this study, I used magnetic field data with HMI to investigate the time evolution and the flux cancellation of the radial component of magnetic field and with SOT/SP to investigate accurately the parameters with the three components of magnetic field.

2.2 Data selection

The criteria of the data selection in this research are

1) There is data set of all the instruments mentioned in **Section 2.1**,

2) The active region is located within +/- 500 arcsec from the disk center when > M-class flares (> 10^{-5} W m^{-2}) happened, and

3) A sigmoidal structure is observed in soft X-rays within 12 hours before the flare of interest happens.

As mentioned in **Section 1**, the target of this research is how much flux is cancelled at the photosphere associated with magnetic reconnection events in the corona and how well multiple reconnection events contribute to the formation of sigmoid. Since the emergence of magnetic flux from below the photosphere is also another source for magnetic reconnection in the corona (Yokoyama & Shibata 1995), it is more suitable to examine the active regions without flux emergence in the period of the sigmoid formation. Moreover, as mentioned in **Section 1.3.1**, active regions formed with flux emergence tend to be complex magnetic structures in the photospheric surface such as δ-type sunspots. A δ-type sunspot is a complex active region in which two umbrae with opposite magnetic polarities are embedded in one penumbra. Therefore, the other criteria of the data selection are

4) Few sunspots increase (i.e., little flux emerges) in the active region

and

5) The whole active region has a bipolar magnetic structure.

In the period from 2006 to 2015, there are 20 events which satisfy the criteria 1), 2), and 3) as shown in **Table 2.1**. As for the criterion 3), I applied the IDL algorithm, developed by ourselves, that identifies bright S or inverse S- shaped bright structure with XRT thin Be images (see **Appendix 1.** in detail). In **Table 2.1**, the column of X-ray class is defined as the peak of soft X-ray flux measured by *Geostationary Orbiting Environmental Satellites* (*GOES*). For examples, X3.4 and M6.3 class correspond to 3.4 $\times 10^{-4}$ $\mathrm{W\,m^{-2}}$ and 6.3 $\times$ 10^{-5} $\mathrm{W\,m^{-2}}$ respectively. The column of sunspot number and the sunspot type are quoted from Solar Monitor webpage (https://www.solarmonitor.org/). The column of sunspot type shows the Mount-Wilson magnetic classification, which classifies sunspots into eight types as the magnetic complexity. These types are $\gamma\delta, \beta\gamma\delta, \beta\delta, \delta, \beta\gamma, \gamma, \beta, \alpha$ in order of magnetic complexity. α-type is defined as a unipolar sunspot group. β-type is defined as a sunspot group having both positive and negative magnetic polarities (bipolar), with a simple and distinct division between the polarities. γ-type is defined as a complex active region in which the positive and negative polarities are so irregularly distributed as to prevent classification as a bipolar group. Earlier studies indicated that the δ-type sunspot groups are highly related to the major flare eruptions (e.g., Zirin & Liggett 1987).

Additionally, for the active regions where the 20 events happened, I calculated the three parameters by using HMI SHARP data just before the onset time of the flare:

a) Total value of vertical component of electric current, which is

$$I_{z,total} = \int_S \mu_0 (\nabla \times \boldsymbol{B})_z \, dS \, ,$$

where μ_0 is magnetic permeability, $\boldsymbol{B}$ is the 3D vector magnetic field, and S is the FOV of the HMI SHARP data.

b) Total unsigned magnetic flux

$$\Phi_{total} = \int_S |\boldsymbol{B}|\, dS\,,$$

c) Average alpha, which is the weighted spatial average value of torsional parameter α. Here α means the ratio of current density $\boldsymbol{j} = \nabla \times \boldsymbol{B}$ to magnetic field strength $\boldsymbol{B}$ (Hagino & Sakurai 2004)

$$\alpha_{z,ave} = \frac{\sum j_z B_z}{\sum |B_z|^2}\,.$$

j_z and B_z are the electric current density and magnetic field strength in the z direction (line of sight). In these calculations, the pixels with weaker magnetic strength, smaller than 200 G, were ignored. These parameters of the 20 active regions are summarized in **Table 2.1** below. NOAA AR 11692 has only a pair of sunspots and relatively small flux in the whole active region. NOAA AR 11882 also has small flux relatively but the average alpha, which represents the averaged twist of magnetic field, in NOAA AR 11882 is nearly twice as that in NOAA AR 11692. For the purpose of this study, only NOAA AR 11692 is proper for this study, because the simplicity of this active region corresponds to little effect of flux emergence to the formation.

Table 2.1 Sigmoidal active regions observed by *Hinode* and *SDO*. Sunspot type: the Mount Wilson magnetic classification; Sunspot number: the number of spots at the day when the flare occurred and the value in the bracket indicates the increased number of spots from one day before the flare; total current $I_{z,total}$, total unsigned flux Φ_{total}, and average alpha $\alpha_{z,ave}$: the values were calculated in the entire area of each active region using HMI SHARP data just before the flare onset. About the M2.0 class flare on 1:02 UT on 21 June), no data of sunspot type and sunspot number can be acquired from Solar monitor.

NOAA No.	Flare start time (UT)	X-ray class	sunspot type	sunspot number	total current [10^13A]	total unsigned flux [10^22Mx]	average alpha [10^-10 /cm]
11158	2011/2/16 1:32	M1.0	βγδ	36(0)	8.02	2.97	4.9
11429	2012/3/9 3:22	M6.3	βγδ	28(0)	15	5.81	-5.21
11692	2013/3/15 5:46	M1.1	β	2(0)	6.28	2.31	-1.23
11882	2013/10/28 14:46	M2.7	βγδ	31(20)	6.1	2.04	-2.36
11890	2013/11/10 5:08	X1.1	βγδ	42(-16)	13.4	4.65	2.37
11967	2014/2/4 1:16	M3.8	βγδ	88(-6)	26.6	9.17	-3.87
12127	2014/8/1 17:55	M1.5	βγδ	10(-2)	25.5	10.7	0.71
12192	2014/10/22 1:16	M8.7	βγδ	66(23)	36.4	15.7	-0.63
12192	2014/10/22 5:11	M2.7	βγδ	66(23)	37.3	15.6	-0.5
12192	2014/10/24 20:50	X3.1	βγδ	58(3)	37.9	17.6	-0.78
12192	2014/10/25 16:55	X1.0	βγδ	62(4)	39.5	19.1	-0.32
12242	2014/12/17 4:23	M8.7	βγδ	25(10)	36.3	13	0.44
12277	2015/2/4 2:08	M1.2	βγ	36(-4)	14.6	4.38	-0.86
12297	2015/3/11 18:37	M1.0	βγδ	32(13)	11.3	3.38	9.09
12297	2015/3/12 4:41	M3.2	βγδ	19(-13)	10.5	3.39	9.4
12297	2015/3/12 21:44	M2.7	βγδ	19(-13)	10.6	3.14	9.83
12297	2015/3/13 3:47	M1.2	βγδ	20(1)	9.91	3.08	10
12297	2015/3/14 4:23	M1.3	βγδ	23(3)	9.52	3.13	7.85
12371	2015/6/20 6:28	M1.0	βγδ	31(5)	11.7	5.34	-2.18
12371	2015/6/21 1:02	M2.0	?	?	10.4	4.97	-2.7

2.3 NOAA AR 11692

NOAA AR 11692 appeared from the east limb on 9 March 2013. On 15 March 2013 at the coordinate of N11E12, an M-class flare started at 5:46 UT and peaked at 6:58 UT on 15 March (see the time evolution of *GOES* flux in the right panel of **Figure 2.2**). An M-class flare means the peak of X-ray flux attained to the range from 10^{-5} to 10^{-4} W m^{-2}. As mentioned in the following **Section 4.1**, an S-shaped structure appeared about three hours before the flare and there seems to be some small brightenings due to the interaction of multiple magnetic field lines before then. I focused on the data taken from 13 March (N09N35) to the flare onset on 15 March (N09E06), in which the active region existed within $\pm$500” from the disk center. In this period, this active region can be seen from above the region in the nearly vertical direction. The FOV of HMI SHARP and SOT/SP are (x, y) ~ (400", 340") and (170", 120") respectively. I used the six SOT/SP maps acquired before the flare (12:01, 15:00, 18:15, 21:00 UT on 14 March, 00:00, and 03:00 UT on 15 March) and a map during the flare (06:35 UT on March), all of which are taken in the fast map mode. XRT acquired focused images of AR 11692 from 11:45 UT on 14 March. As for the period when no XRT data was acquired, thus AIA data is used in the following analyses. HMI and AIA data can be acquired except for the eclipse period (around 6:30-7:30 UT in March).

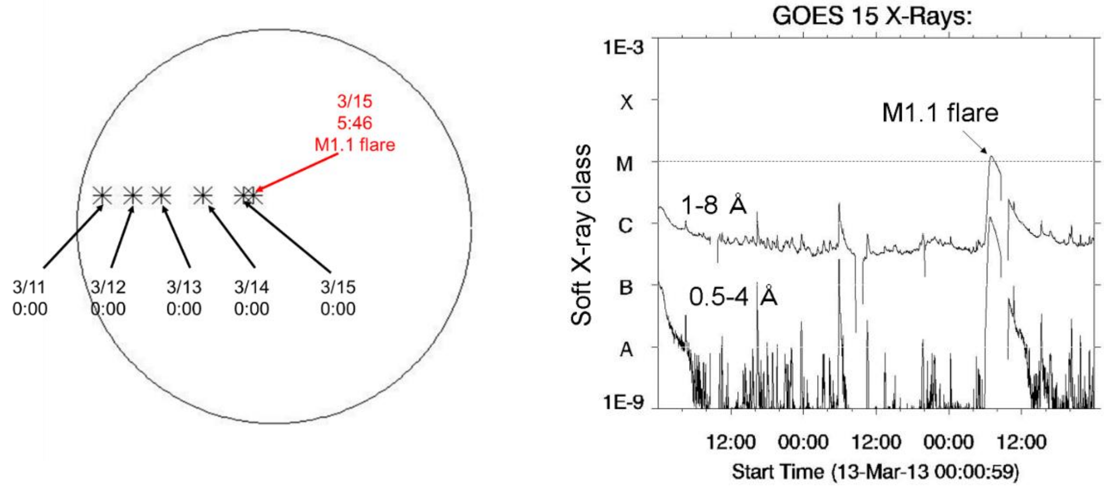

Figure 2.2 Left: Asterisk points are the positions of NOAA AR 11692 at from 11 March to the onset of M1.1 flare. The circle means the solar limb. Right: Soft X-ray flux from the sun measured by *GOES* in the 1-8 Å channel (upper line) and the 0.5-4 Å channel (lower line). The y-axis indicates soft X-ray flux [W m^{-2}] in a logarithmic scale.

3. Data analyses and Methods

3.1 Data calibration

In this study, I used sets of the data acquired by four space-borne different telescopes. This subsection describes the calibration of these data.

3.1.1 Corrections for dark current, flat field, cosmic rays, and exposure normalization

All the XRT level 0 (i.e., raw data) images were calibrated by the standard procedure *xrt_prep.pro* available in the *Solar SoftWare*. The calibration corrects dark current level, flat field, removal of high intensity pixels caused by cosmic rays. The images are also normalized with the exposure duration. Note that *xrt_prep.pro* also removes orbital variation (a few arcsec variation) in pointing coordinate information and makes time series of XRT data co-aligned each other. The calibrated AIA data (level 1 data), which has been de-spiked, flat-fielded and the dark current and CCD pedestal removed, was available for my use. The procedure *hmi_prep.pro* was used to perform image registration (rotation, translation, scaling) of AIA Level 1 images and update the header information. By applying this procedure, the HMI full disk images are co-aligned to HMI SHARP full-disk maps with the accuracy better than a few arcsecs.

3.1.2 Corrections for solar rotation and extraction of ROI from AIA full-disk images

I used the time series of AIA full-disk images, from 0:00 UT on 13 March to 6:00 UT on 15 March, which were taken at a time cadence of 2 minutes. In order to extract the region of interest (ROI) moving with the solar rotation, I needed to get the coordinate of the center of the ROI at the time of each AIA image. At first, I set the center coordinate of ROI (x, y) = (-568.8", 241.2") at 0:00 UT on 13 March, which is the time of the first AIA image. The ROI, of course, contains the whole structure of NOAA AR 11692. I applied *tim2carr.pro,* which is a procedure in IDL *SolarSoftware* and enables to refer the Carrington rotation number. Based on the difference between the values of the Carrington rotation numbers, I derived the center coordinate of ROI at each image. The scale of ROI in all the AIA full-disk images is set 360” and 360” in the north-south direction and the east-west direction respectively.

3.1.3 Co-alignment of images from the different instruments

SOT/SP continuum intensity data was co-aligned with a nearby XRT G-band data by using the coordinate offset which is derived from the maximization of cross-correlation coefficient between SOT/SP continuum data and XRT G-band data, since both of them contain umbral and penumbral structures. In order to co-align SOT/SP magnetic data with XRT coronal images, we also corrected for the XRT internal offset between G-band and X-ray reported by Shimizu et al. (2007). For the co-alignment between XRT and AIA, the offset was derived from the maximization of cross-correlation coefficient between AIA 1600 Å image and XRT G-band image, both of which contain the sunspot. As for the magnetic field data of SOT/SP and *SDO*/HMI, I also co-aligned them by the maximization of the cross-correlation coefficient between the field strength maps of SOT/SP and HMI SHARP. Those calculations of cross-correlation coefficients and the incident offset are derived by the IDL routine *get_correl_offsets.pro*. **Figure 3.2** shows the chains of co-alignment between data set from different instruments. There is a gap of a few pixels in north-south and east-west axis between the HMI SHARP image which is co-aligned with XRT G-band via SOT/SP maps (left side of chains in **Figure 3.2**) and the AIA image which is co-aligned with XRT G-band via AIA 1600 Å (right side of chains in **Figure 3.2**). Thus, I finally corrected for the gap by eye after these set of the automatic co-alignment processes.

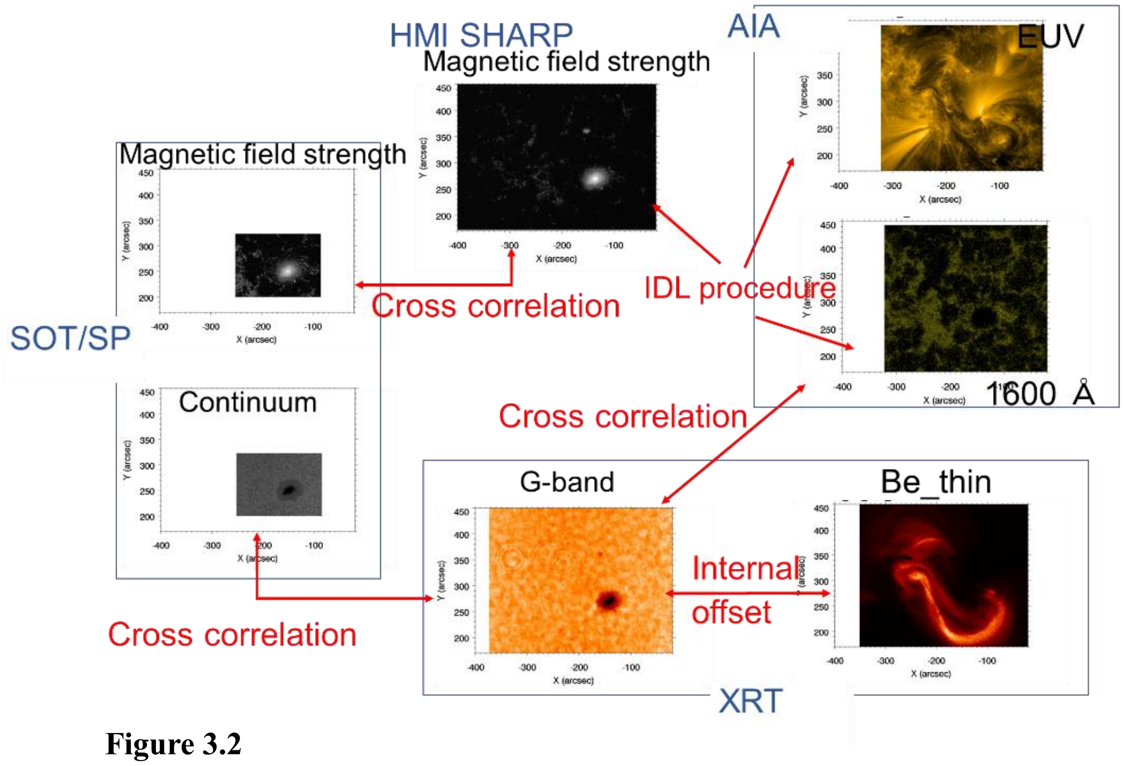

Figure 3.2

The chains of co-alignment between data set from different instruments. These seven images are acquired at the same time and drawn in the same scale.

3.1.4 Removal of 180 degree ambiguity

All of the qualification of the vector magnetic field making use of Zeeman effect has an intrinsic problem 180 degree azimuth ambiguity, i.e. it does not distinguish the two horizontal directions of magnetic field, θ and θ + 180°, which has to be resolved before the analysis of vector magnetic field data. Some methods for resolving the azimuth ambiguity are currently available; their details can be found in a review article by Metcalf et al. (2006). In this study, I used the *AZAM* procedure, which provides the manual solution. In the *AZAM*, at first one corrects the horizontal vector on the condition of $\boldsymbol{B}_{\mathbf{pot,t}} \cdot \boldsymbol{B}_{\mathbf{obs,t}} > 0$, where $\boldsymbol{B}_{\mathbf{obs,t}}$ is the transverse or horizontal component of the observed field, and $\boldsymbol{B}_{\mathbf{pot,t}}$ is the horizontal component of the extrapolated potential field, which satisfies $\nabla \times \boldsymbol{B} = \mathbf{0}$. After that, I also manually corrected the direction by smoothing in small regions (2 x 2 pixels) in which there is a pair of almost anti-parallel vector elements. As for AR11692, SOT/SP level2 data does not contain the whole active region, thus before the extrapolation of the potential field, the rest region had to be complemented with HMI magnetic data, which has a larger FOV than that of SOT/SP.

3.2 Physical parameters

In this subsection, I show what and how physical parameters were derived from the data set.

3.2.1 Magnetic cancellation flux

The amount of flux cancelled is calculated from the reduction in total magnetic flux in a small box. The position of the box is defined as where small elements of positive and negative flux collide each other at the time when a reconnection event happened in the corona. The HMI SHARP, however, gives us "magnetic flux density" of three directions while the area of each pixel in the solar surface is different because the spatial cadence of pixels is set to the constant value of arcsecond (~0.5"). Thus, in order to derive "magnetic flux", "magnetic flux density" has to be multiplied by the area of each pixel thinking of the heliographic coordinate of each pixel.

3.2.2 Magnetic shear angle

Sigmoid is a signature of non-potential, magnetic field structure in the corona. Since the magnetic field lines involved in the sigmoid are rooted in the solar surface (photosphere), some signatures of the magnetic non-potentiality may be observed at the photosphere, where accurate measurements of magnetic field vectors available from SOT/SP observations. In order to identify such non-potential features at the photospheric level, I calculated the difference between the observed magnetic field vector and the potential field vector. The potential field vector was extrapolated with the procedure *fff.pro*, which is available in the NLFFF (nonlinear force-free field) package of the *SolarSoft* library. Two parameters related to the angle difference, i.e., twist shear angle and dip shear angle, are used. The twist shear is defined as the deviation from the direction of the potential field on the solar surface plane, which is the difference in the horizontal component between the potential field ($\boldsymbol{B_{ph}}$) and the observed field ($\boldsymbol{B_{oh}}$):

$$\Delta\psi = \cos^{-1}\frac{\boldsymbol{B_{oh}} \cdot \boldsymbol{B_{ph}}}{|\boldsymbol{B_{oh}}||\boldsymbol{B_{ph}}|}$$

The relation shown in the left panel of **Figure 3.3** gives positive value. On the other hand, the dip shear is the difference of the horizontal component. The relation of the direction of magnetic field and shown in the right panel of **Figure 3.3**. Dip shear $\Delta\gamma$ is defined as

$$\Delta\gamma = \gamma_o - \gamma_p,$$

when γ_o and γ_p is the inclination angle of the observed and the potential field vector respectively. Positive sign of dip shear means that the observed magnetic field vector is more horizontal than the potential field vector. It should be noted that the term "shear" means observational shear and we should not confuse it with the term "shear" used as actual shear in studies on solar magnetism (e.g., shear motion).

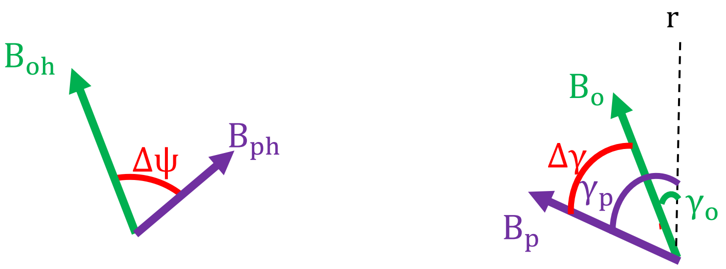

Figure 3.3 The relation of the directions of magnetic field and the shear angle. Left: $\boldsymbol{B_{oh}}$ and $\boldsymbol{B_{ph}}$ correspond to the horizontal component of observed and potential magnetic field respectively. Right: $\boldsymbol{B_o}$ and $\boldsymbol{B_p}$ correspond to the vector of observed and potential magnetic field respectively seen in the vertical plane.

Physically, the dip shear can be understood in terms of azimuthal currents, in the same way as the twist shear can be understood in terms of axial currents. Larger values of these angles mean that the non-potentiality of the AR is larger. It may be noticed that, unlike the twist shear, the dip shear is not affected by the 180◦ azimuth ambiguity, if the AR is observed close to the disk center. The penumbral area close to the flaring site shows a high value of the twist shear and dip shear as compared with other parts of the penumbra (Gosain & Venkatakrishnan 2010).

4. Results

4.1 Sigmoidal structure

Figure 4.1 shows the time evolution of the coronal loop structures recorded in XRT images. At 11:45 UT on 14 March, which is the time when the first XRT image was taken for AR11692. There was an initially I-like bright feature (J1 in **Figure 4.1** (a)) in the northeast part of AR11692 and then J1 became a J-shaped. At 21:41, about 9 hours prior to the flare, the other J-shaped bright feature (J2 in **Figure 4.1** (b)), the straight part of which was almost parallel to that of J1, suddenly appeared in the southwest part of AR11692. Note that this J-shaped bright feature has already been visible as faint structures in **Figure 4.1** (a). Around 3:17 UT on 15 March, about 3 hours before the flare, an S-shaped bright feature was clearly observed (**Figure 4.1** (c)). The J2 structure may be developed to form this S-shaped bright feature. The northern end of J2 structure is co-spatial to that of J1 structure. At the onset of the flare, only J2 was brightened and then erupted as a halo CME (**Figure 4.1** (e)).

Since a former coronal structure to be visible as the J-shaped bright structure later can be recognized, although very faint, in the XRT first image taken at 11:45UT on 14 March, I also examined AIA coronal images acquired before that time to understand how pre-J-shaped structure was created in earlier period. As briefly described in **Section 2.1.1**, AIA records different temperature components of the plasma in the corona by using various kind of EUV and UV bands. Thus, I examined AIA images taken with different bands and found that the former structure of J2 can be seen in 171 Å images. The former structure of J2 before the X-ray sigmoid evolution can be seen in 171 Å. At 1:13 UT on 13 March, there was a small potential-like arcade (**Figure 4.2** (a)) and the arcade was elongated in the southwest direction (**Figure 4.2** (b), (c)). From around 0:00 UT on 15 March, the elongated arcade became less visible in 171 Å (**Figure 4.2** (d)) while J2 became more visible in soft X-ray. Thus, this cooler arcade structure may correspond to the former structure of J2. Here, this arcade was rooted in the positive and negative magnetic field seen in the HMI magnetogram (compare **Figure 4.2** (a-d) with **Figure 4.2** (e)). In the evolution from the arcade to J2, multiple sudden brightenings appeared, as shown in **Section 4.3** in detail.

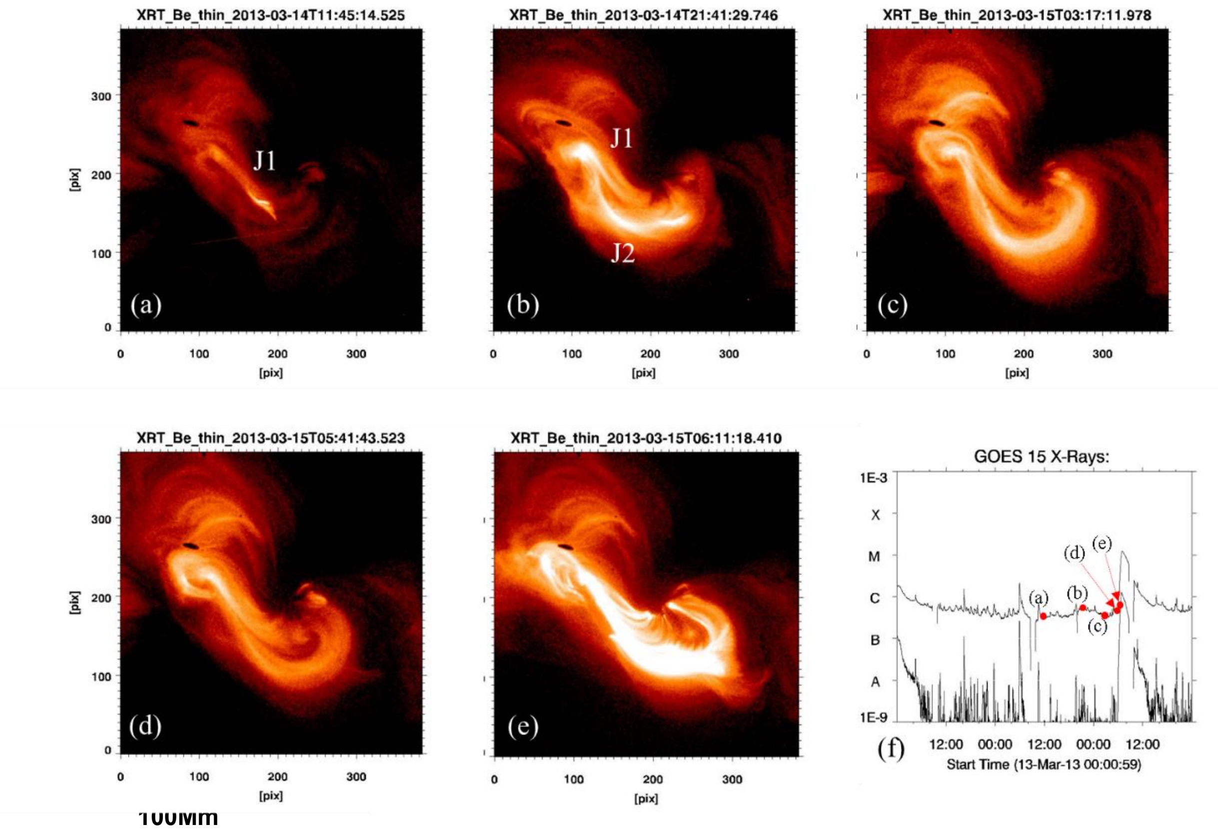

Figure 4.1

(a-e) The coronal structure from XRT observation at different times. (f) The time plot of the *GOES* X-ray flux. The upper and lower lines indicate the full-sun soft X-ray flux through 1–8 Å and 0.5–4 Å, respectively. Red points indicate the timing when the image in each panel was acquired.

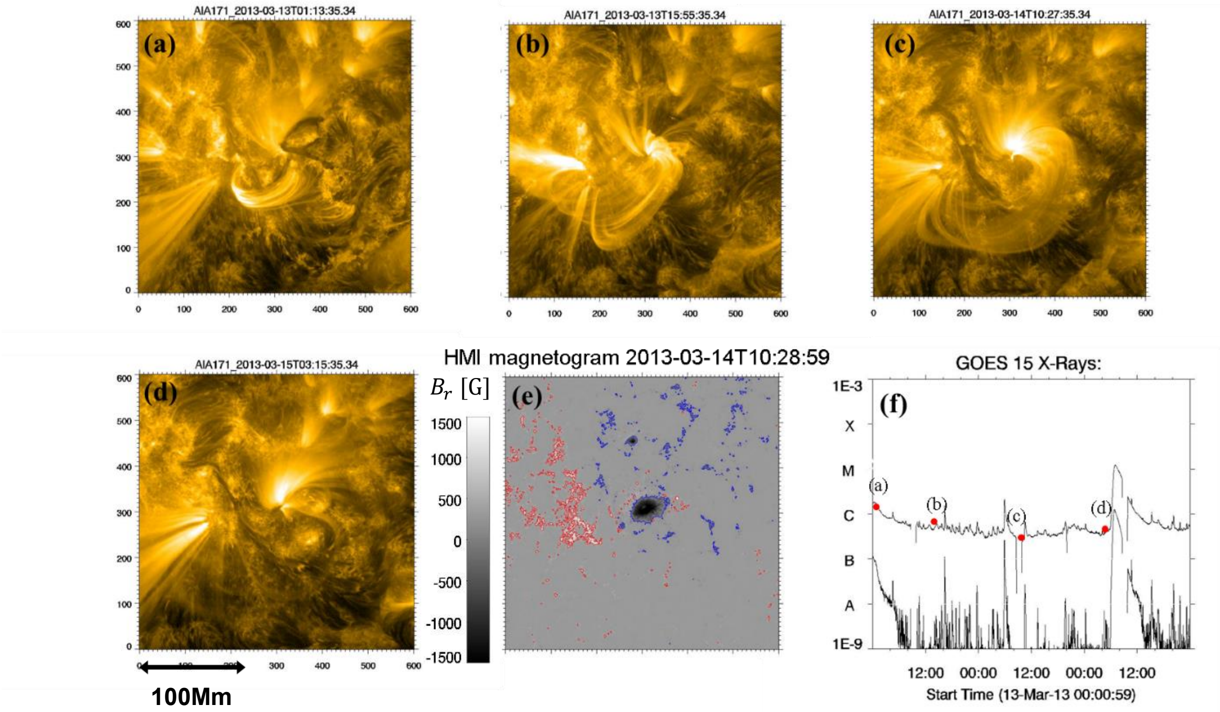

Figure 4.2 (a-d) Coronal structures visible with low temperature (~ 1 MK) plasma from AIA 171 Å observation. (e) Line of sight component of photospheric magnetic field. The color of background white and black indicate upward and downward direction respectively. Red and blue contours indicate 100 and -100 Gauss respectively. (f) Plot of the *GOES* X-ray flux. The upper and lower lines indicate the full-sun soft X-ray flux through 1–8 Å and 0.5–4 Å, respectively. Red points indicate the timing when the image in each panel was acquired.

4.2 Signature of magnetic non-potentiality at the photospheric level

As shown in **Section 4.1**, from 13 March a J-shaped loop bundle J2 developed and became a part of the sigmoidal feature. In this subsection, I show where the footpoint of J2 was located, whether the non-potentiality of magnetic field existed, and how it evolved with estimating the physical parameters.

4.2.1 General description of photospheric magnetic field

Figure 4.3 shows the radial component of the photospheric surface magnetic field (HMI SHARP data) at 23:58 UT on 12 March 2013 and 06:10 UT on 15 March 2013, which are the start time and end time respectively of the data used in this study. The color white and black correspond to positive (the upward field from the surface) and negative (the downward field from the surface) magnetic polarities respectively. The photospheric magnetic structure in AR11692 consists of a leading negative sunspot and a following positive one, i.e. β (bipolar) magnetic configuration, according to the Mount-Wilson sunspot magnetic classification. The former looks well-organized while the latter is sporadic. Morphologically, the global structure of the sunspots and the main photospheric magnetic field does not change in all the period. The total magnetic flux in the whole AR 11692 decreases mainly by the decrease of the flux near the PIL (see **Figure 4.4**). $|B_r| < 50$ G is ignored in this summation in order to overcome the error of data. In the initial period (13 March), AR11692 is far from the disk center thus the unsigned flux is not so accurate. The positive flux with weak magnetic field may be ignored. From negative flux at 15 March ($\sim 4 \times 10^{20}$ Mx) nearly corresponds to the unsigned flux in the whole AR 11692. The decrease of the total unsigned flux is $\sim 2.5 \times 10^{20}$ Mx.

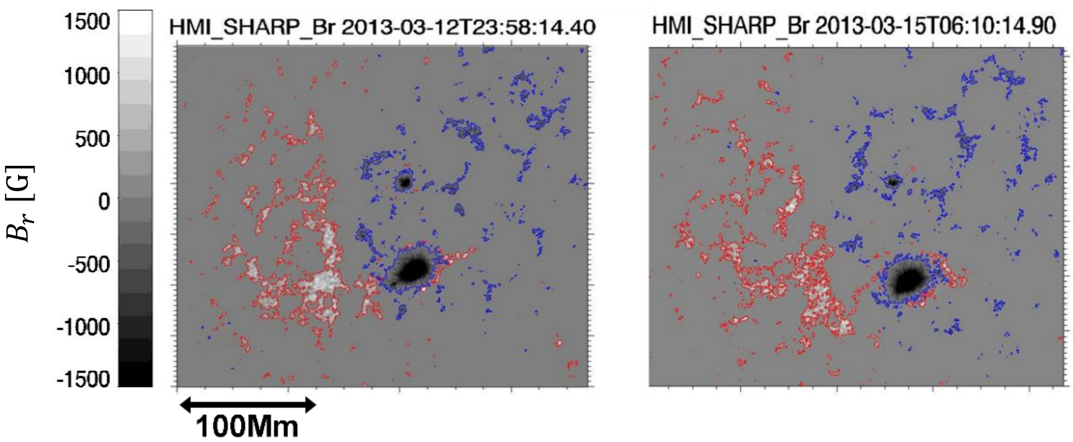

Fig 4.3 Radial component of magnetic field at the photosphere in NOAA AR 11692 acquired by HMI SHARP. Background colors white and black are positive and negative magnetic polarities respectively. Contours indicate 100 (red) and -100 (blue) gauss respectively. The times of two data are 23:58 UT on 12 March 2013 (left) and 06:10 UT on 15 March 2013 (right). These plate scales are almost same (~ 0.5”).

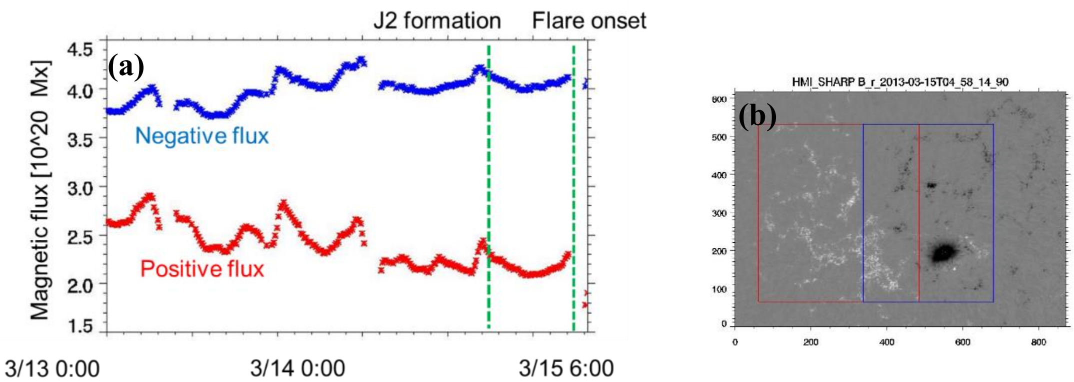

Figure 4.4 (a) Time evolution of the total magnetic flux of positive (red) and negative (blue) magnetic elements. The spatial ranges of these summations are shown as the red and blue rectangles in the panel (b). The vertical broken lines represent the times of the J2 formation and the flare onset.

4.2.2 The position of the sigmoid footpoint in the negative sunspot

When the flare started, a part of the sigmoidal structure was brightened in soft X-ray, as seen in **Figure 4.1** (e). Transient chromospheric brightenings, i.e., flare ribbons, appeared in respond to the X-ray brightening. Thus, the location of flare ribbons can be used to identify where the footpoint of sigmoid is located at the photosphere. Flare ribbon can be identified in SOT/FG Ca II H line. **Figure 4.5** (a) shows a map of SOT/FG Ca II H line intensity at 6:11 UT on 15 March 2013, when J2 was erupting. A bright feature is located at the west part of the sunspot. The data of the Ca II H line intensity is acquired in the time cadence of 1 minute and the movie around the onset time indicates the bright feature, which is the flare ribbon, moved from the south-west part of the sunspot. In **Figure 4.5** (b), the red region indicates where the running difference of the intensity from 5:46 to 6:11 exceeds a threshold, while the blue region indicates where in the penumbra the change of the intensity was not significant from 5:46 to 6:11. It is noted that the chromospheric filament observed in Hα showed active motions before the onset of the flare (6:11 UT) and thus the filament activation may be related to the movement of red regions from the south-west to the north-east. **Figure 4.6** shows the relation of the positions between the coronal loop appeared in soft X-ray and the sunspot. The bright bundle J2 should be rooted at the almost west part of the sunspot, although it is not so accurate because the lower boundary of the corona, which is the layer soft X-ray is sensitive, is diffuse and ~ 2000 km higher than the level of the photospheric surface. If the pre-eruptive configuration J2 was reconnected with ambient field from higher part of J2 to lower part, the movement of the red region can be understood. These features, therefore, indicate that the footpoint of J2 should be located in the west part of the penumbra.

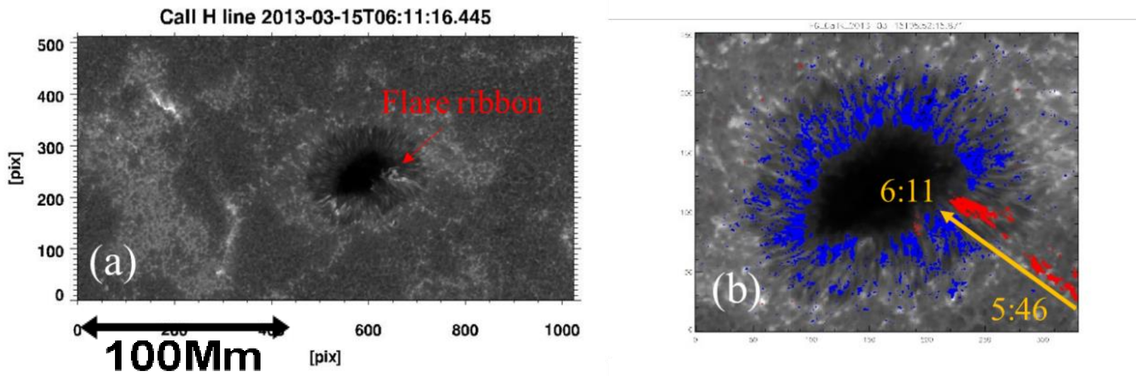

Figure 4.5

(a) SOT/FG Ca II H line intensity at 6:11 UT on 15 March 2013. (b) Background is same as panel (a) but for around the main sunspot. Red region indicates the region where the running difference from 5:46 to 6:11 exceeds 50DN. Blue regions indicates the region where the increase of intensity from the data at 1 minute is always under 20 DN in the time range from 5:46 to 6:11.

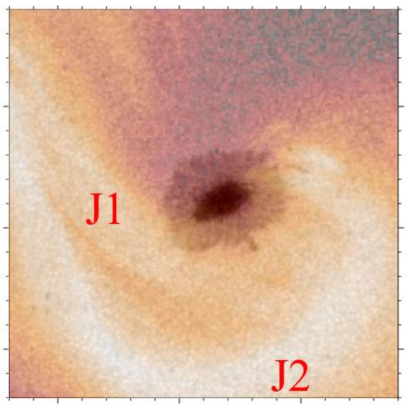

Figure 4.6

SOT/SP continuum intensity map overlaid by the image of XRT coronal loops at 2:57 UT on 15 March.

4.2.3 Magnetic shear angle

In this subsubsection, I show the signature of non-potentiality, i.e., dip shear angle and twist shear angle, defined in **Section 3.2.2**, in the region around the footpoint of J2, identified in **Section 4.2.2.** I derived twist shear angle and dip shear angle around the leading negative sunspot from SOT/SP magnetic data taken at 11:58, 14:58, 18:10, 20:58, and 23:58 UT on 14 March, 02:58 and 06:10 UT on 15 March. The region where I derived them is same as shown in **Figure 4.7**. The spatial distributions of dip shear and twist shear for the seven data are shown in **Figure 4.8** and **Figure 4.9**. The data before the formation of J2 in **Figure 4.8** and the data after the formation are shown in **Figure 4.9**. The notable features of these figures are;

1. Dip shear in the west part of the umbra is basically negative and lower than that in the ambient region (see the region R3 in **Figure 4.8** (a1) and the corresponding regions of panels of left column of **Figure 4.8** and **Figure 4.9**). At the flare onset, these features are slightly weakened (see panels (f1) and (g1) in **Figure 4.9**).

2. Twist shear in the penumbra is generally negative (see the blue region of panels (a2-g2) of **Figure 4.8** and **Figure 4.9**).

3. Twist shear is negative and lower than -10 degrees in two regions in the penumbra; the northeast part and the west part of the sunspot (see the region R1 and R2 in **Figure 4.8** (a2) and the corresponding regions of panels (a2-g2) of **Figure 4.8** and **Figure 4.9**).

These features will be interpreted in **Section 5.1** focused on the region R1, R2, and R3.

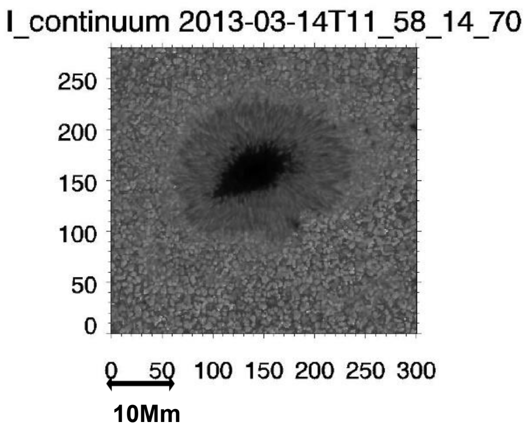

Figure 4.7

The map of continuum intensity around the main sunspot. This window is same as the following panels of **Figure 4.8** and **Figure 4.9**.

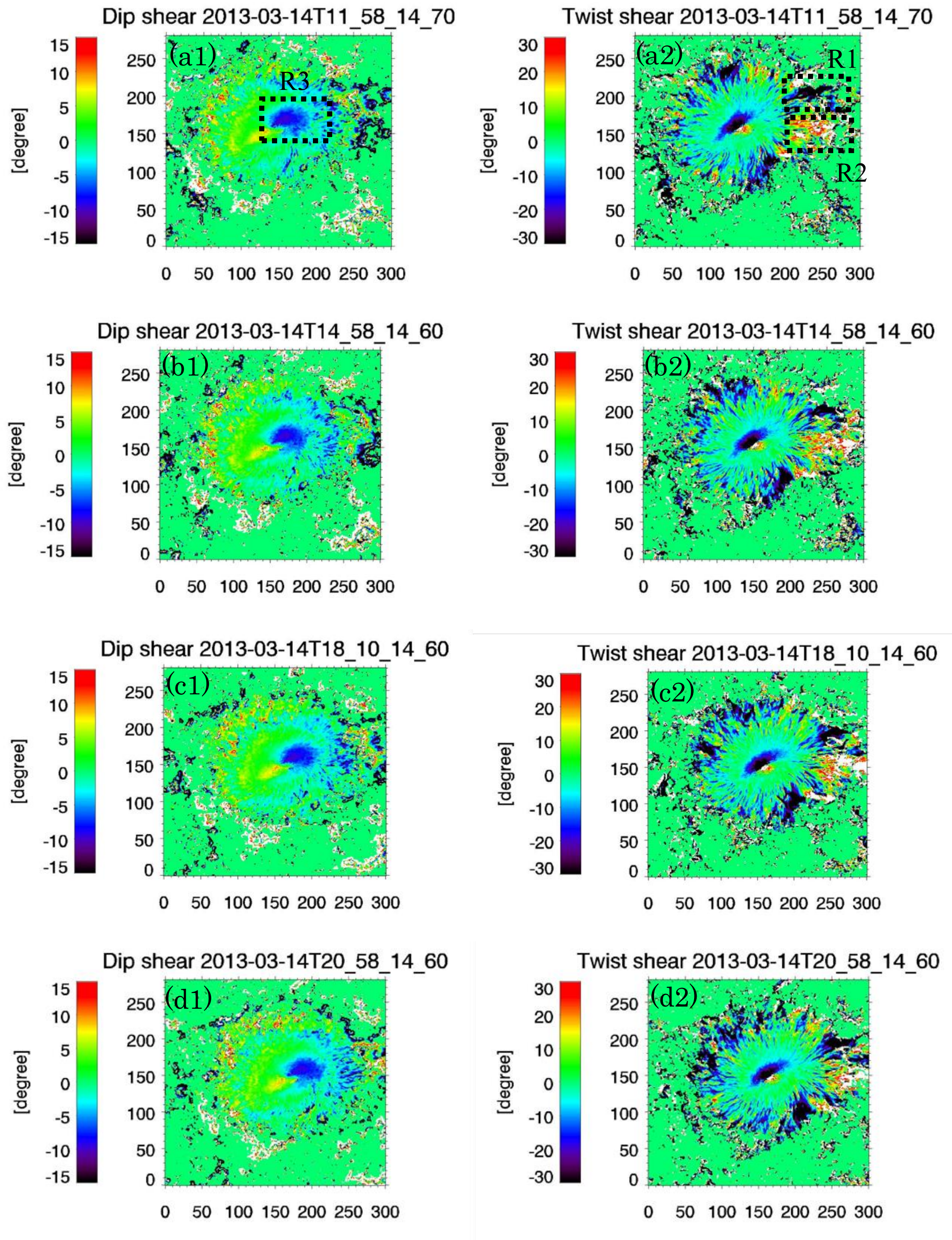

Figure 4.8

Maps of dip shear angle and twist shear angle before the formation J2. The broken rectangles in panels (a1) and (a2) indicate the regions where the notable features are.

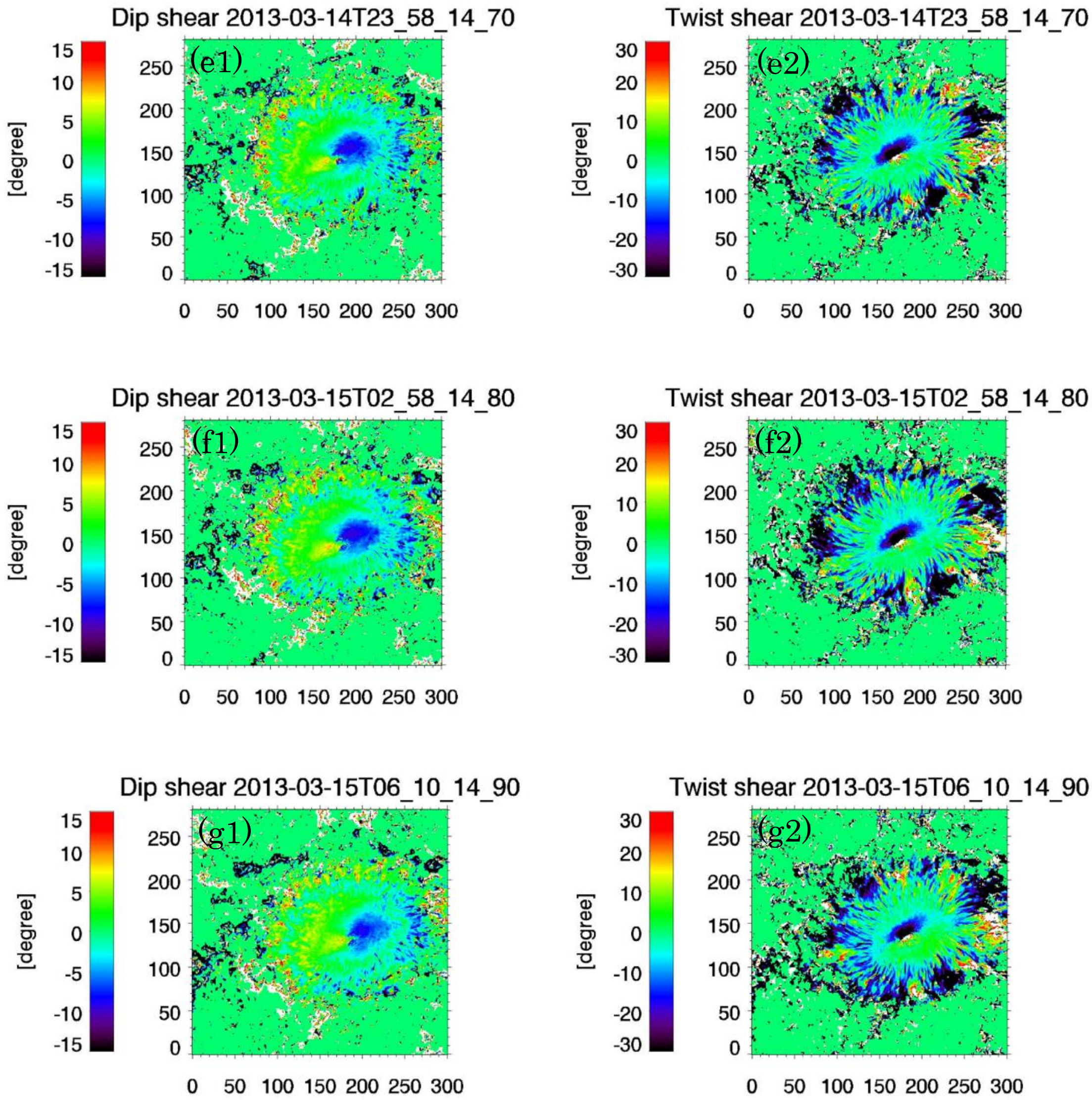

Figure 4.9

Same as **Figure 4.8** but after the formation of J2.

4.3 Reconnection events and magnetic cancellation

As shown in **Section 4.2**, the pre-eruptive configuration J2 should be non-potential, twisted and/or sheared, structure. In the time range of the formation of J2, there was little flux emerged. As described in **Section 1.3**, magnetic reconnection events in the atmosphere can be contribute to the formation of the pre-eruptive configuration other than flux emergence. In this subsection, I focus on the possibility of the formation process and show its evidence observationally.

4.3.1 Magnetic structure related to the reconnection events

Dark filaments are important observational features of magnetic structure near the PIL. Filaments are cool and dense plasma in the hot and tenuous atmosphere. Filaments can be seen in Hα and 304 Å (He II line) as dark thread features. The magnetic structure of filaments is usually thought to be sheared arcades on the PIL (Antiochos et al. 1994; Aulanier et al. 2006), which possess magnetic dips which can provide an upward magnetic tension against the gravity of filament materials (Mackay et al. 2010; Martin 1998). The formation process of filaments is also suggested to be via magnetic reconnection (Kaneko & Yokoyama 2015)

The panels of **Figure 4.10** show the AIA 304 Å images of the ROI, defined in **Section 3.1.2**, at 13:43 UT on 13 March and 10:07 UT on 14 March, both of which were acquired when J2 is formed. The images and the movie of AIA 304 Å indicates that there are two dark thread bundles almost along the PIL and they get coalesced gradually as J2 is formed. These processes of coalescence should be associated with a series of magnetic reconnection events.

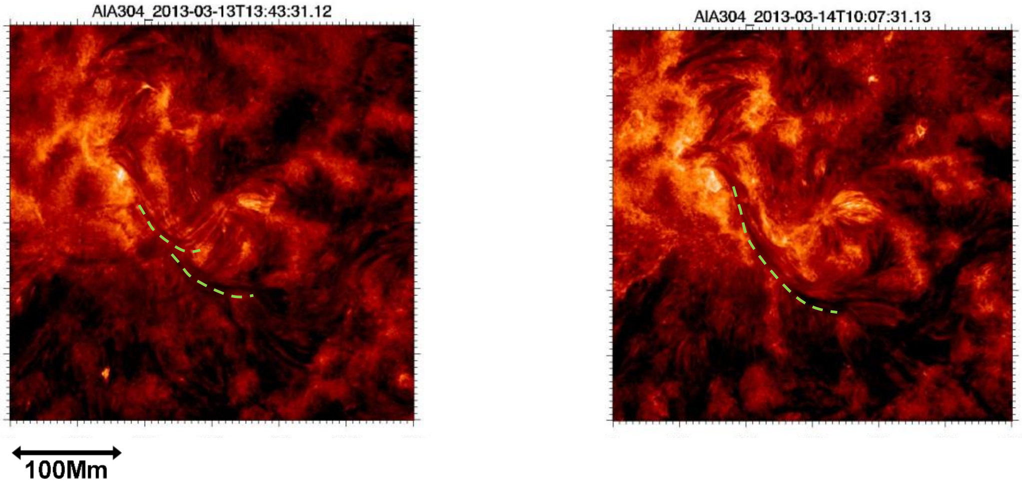

Figure 4.10

AIA 304 Å images of the ROI at 13:43 UT on 13 March (left) and 10:07 UT on 14 March (right). The yellow-green broken lines indicate the locations of dark filament threads related to the reconnection events.

4.3.2 Coronal brightenings associated with the reconnection events

When J2 was formed, multiple numbers of transient brightenings were observed around the PIL in AIA 131 Å, which is sensitive to hotter plasma, and the bright features elongated in the northeast and southwest directions in several minutes. These transient brightenings mean the creations of heated plasma associated with magnetic reconnection events. One of the brightenings is shown in **Figure 4.11.** The time evolution of AIA 131 Å intensity on the slit S1 perpendicular to the PIL, shown in the right panel of **Figure 4.11**, is shown in **Figure 4.12**. Eighteen brightening events are observed in the time range of the formation of J2. For convenience, I named them MRX1, MRX2, …, and MRX18 from earlier to later, which is indicated by the yellow arrows in **Figure 4.12.**

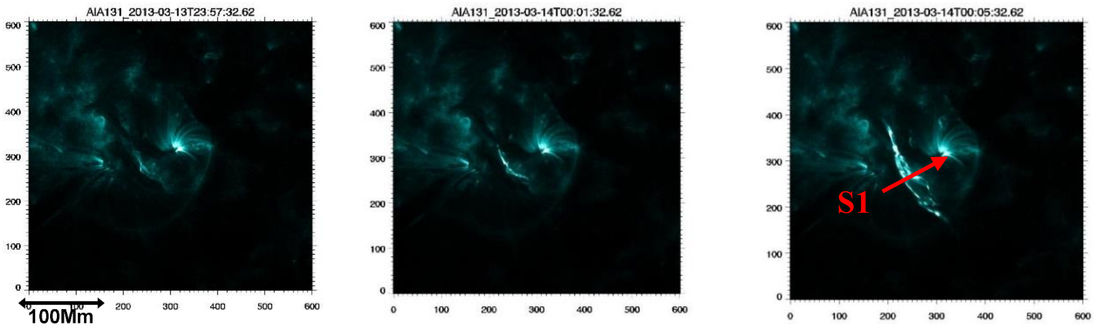

Figure 4.11 AIA 131 Å images of ROI at the time of MRX9 (left), which occurred at 23:57 UT on 13 March 2013, 4 minutes after MRX9 (center), and 8 minutes after MRX9 (right) .

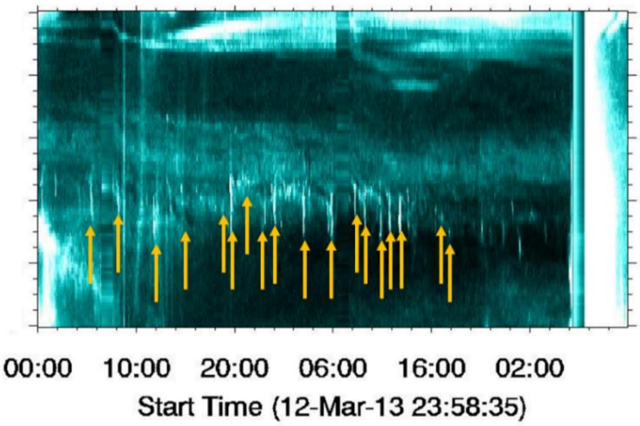

Figure 4.12 Time evolution of the AIA 131 Å intensity at the slit S1 which is shown in **Figure 4.11.** The yellow arrows indicate the times of the reconnection events MRX1, MRX2, …, and MRX18 from left to right.

4.3.3 Magnetic cancellation in the photosphere associated with the reconnection events

In this subsubsection, I show the temporal evolution of the magnetic flux at the photosphere in the vicinity of the 18 reconnection events identified in **Section 4.3.2**. If the magnetic flux is decreased with time, it is considered as magnetic cancellation events. The magnetic cancellation is expected as the consequence of the submergence of magnetic fields due to the magnetic reconnection occurring in the higher atmosphere.

At first, the total flux in the whole AR11692 decreased. **Figure 4.4** shows the time evolution of the total flux of positive (red) and negative (blue) magnetic elements in the active region. The positive flux was monotonically decreased in the period when multiple numbers of reconnection events were observed (between 05:20 UT on 13 March and 17:41 UT on 14 March). The amount of the decreased flux is 6×10^{20} Mx. After 17 UT on 14 March, the positive magnetic flux is almost constant. The negative flux stayed in the range in 2-4 $\times$ 10^{20} Mx, although small variation (increase and decrease) can be seen in the evolution.

What kinds of magnetic activities cause the decrease in the photospheric magnetic flux? How are the magnetic activities at the photosphere associated with the occurrence of magnetic reconnection events? To answer these questions, I investigated the evolution of magnetic flux in the vicinity of reconnection events at the time around the occurrence. For example, MRX2, which is occurred at 9:09 UT on 13 March at the location indicated by a yellow rectangle in **Figure 4.13**. Associated with this event, a magnetic cancellation was identified at the photosphere in the HMI magnetic flux data**.** **Figure 4.14** shows the spatial distribution of the vertical magnetic flux in the yellow rectangle defined in **Figure 4.13** at three different times: at the time of the occurrence of MRX2, 36 minutes after the occurrence, and 84 minutes after the occurrence. Red and blue contours in **Figure 4.14** indicate 50 and -50 G respectively. The magnitude of noise in the HMI magnetogram is in order of 30 G. Thus, the total magnitude of negative magnetic flux was derived by using the pixels with the magnitude lower than -50 G in the rectangle. The resulting time evolution of negative mangetic flux in the yellow rectangle is shown in **Figure 4.15**. The plot indicates the decrease of 0.22×10^{18} Mx in 110 minutes after MRX2. As seen in **Figure 4.3**, some positive magnetic patches are located in the vicinity defined by the yellow rectangle, and they are in a fairly close distance to the large sunspot. Thus, the flux decrease in this region can be interpreted as a magnetic cancellation of a part of positive polarity patches with the negative flux at the eastern edge of the leading sunspot.

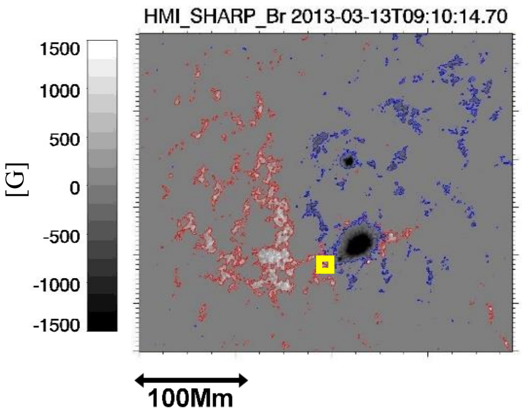

Figure 4.13

The spatial distribution of radial component of the magnetic field (HMI SHARP) at the time of MRX2 (09:10 UT on 13 March). The red and blue contours indicate 100 and -100 G respectively. The yellow rectangle indicates the region where the total flux is summed.

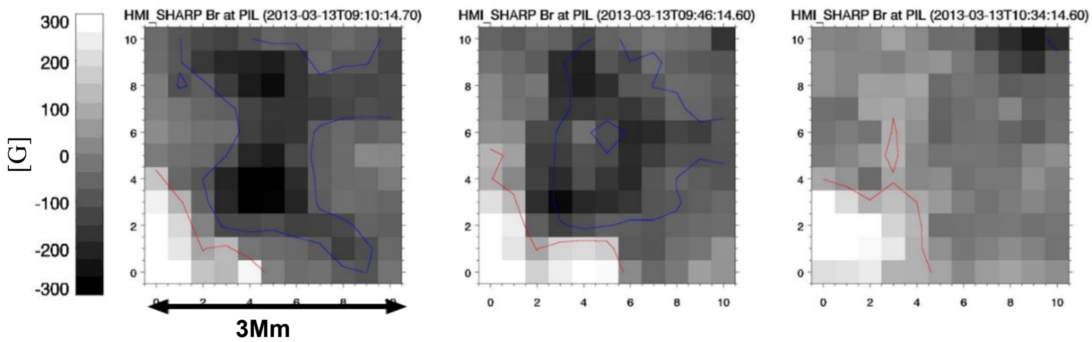

Figure 4.14 The spatial distribution of radial component of the magnetic field in the region shown as the yellow rectangle in **Figure 4.13** at the time of MRX2 (left), 36 minutes after MRX2 (center), and 84 minutes after MRX2 (right). The red and blue contours indicate 50 and -50 G respectively.

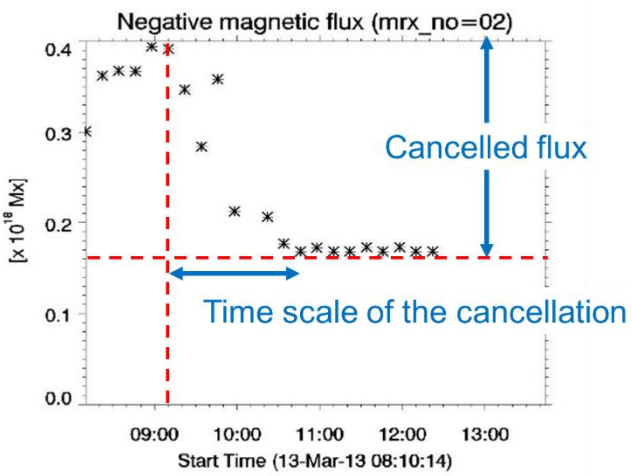

Figure 4.15

Time evolution of negative flux in the region shown in **Figure 4.14.** Flux in the pixels where $|\boldsymbol{B}_r| < 50\mathrm{G}$ is ignored in the summation of flux because of signal noise.

Figure 4.16 shows the location of the 18 magnetic reconnection events on the HMI magnetogram taken at 17:41 UT on 14 March. The first half of the events are given by red, while the last half of the events are given by blue. This figure clearly shows that the position of magnetic reconnection events was slowly moved along the PIL, where magnetic cancellation events took place. The magnetic reconnection events observed in the corona and their corresponding cancellation of magnetic flux at the photosphere are summarized in **Table 4.1.** The position of each magnetic cancellation is given in the coordinate in which flux island, such as blue contour in **Figure 4.14**, vanished. The time scale gives how long the flux decrease was observed in the temporal evolution. The total amount of canceled flux is 7.69×10^{18} Mx.

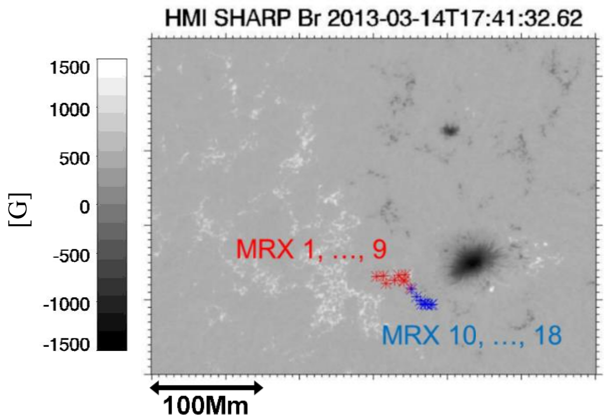

Figure 4.16
The asterisks indicate the positions of the magnetic cancellation events. The colors red and blue of these asterisks mean the positions of from MRX1 to MRX9 and those from MRX10 to MRX18 respectively.

Table 4.1

Multiple reconnection events and cancellation flux. The columns of x and y represent the distance from the cancellation sites to the center of FOV of HMI SHARP.

	date(UT)		x [Mm]	y [Mm]	cancelled flux [10^18Mx]	time scale [s]
MRX1	2013/3/13	05:20	-1.818	-49.9	1	-
MRX2	2013/3/13	09:09	-0.443	-47.3	0.22	6600
MRX3	2013/3/13	11:43	-0.873	-54.4	0.6	7200
MRX4	2013/3/13	14:29	4.293	-50.3	0.6	2160
MRX5	2013/3/13	19:31	2.09	-43.6	0.15	5400
MRX6	2013/3/13	19:57	7.091	-49.6	0.9	8640
MRX7	2013/3/13	21:57	5.781	-42.1	0.13	6480
MRX8	2013/3/13	22:59	3.699	-47.7	0.24	5760
MRX9	2013/3/13	23:53	9.819	-54.1	0.8	5760
MRX10	2013/3/14	02:53	8.072	-54.1	0.55	7920
MRX11	2013/3/14	05:39	10.78	-61.2	0.8	-
MRX12	2013/3/14	08:05	13.04	-63.1	0.3	6000
MRX13	2013/3/14	09:11	12.99	-66.8	0.25	6480
MRX14	2013/3/14	10:37	16.06	-65.7	0.3	7200
MRX15	2013/3/14	11:37	15.61	-65.7	0.35	7920
MRX16	2013/3/14	12:39	16.34	-66.5	0.17	6480
MRX17	2013/3/14	16:35	18.82	-65	0.27	3600
MRX18	2013/3/14	17:41	19.52	-64.2	0.06	4320

5. Discussions

There were two bundles of filament threads at the initial phase of the formation (on 13 March) and their brightenings associated with reconnection events in these threads occurred. As the reconnection events occurred, the threads seem to be coalesced gradually. This fact can be applied to the flux cancellation model suggested by van Ballegooijen & Martens (1989) , introduced in **Section 1.3.2**. The process of flux cancellation can be separated to the two following steps. The first reconnection steps build longer loops from already sheared loops that are significantly aligned with the PIL (see the panel (c-d) of **Figure 1.5**). These loops do not possess any dips. The second step of the process brings footpoints of overlying loops very close together at the PIL, which reconnect to produce long field lines which are twisted around the sheared field (see the panel (e-f) of **Figure 1.5**). In both steps, the reconnection also produces short field lines that get submerged under the photosphere due to magnetic tension so that while a flux rope is forming in the corona there is a corresponding disappearance of flux in the photosphere. Savcheva et al. (2012) suggests in this scenario axial flux gets built up first, followed by poloidal flux, and the two fluxes sum to at most the total cancelled flux.

In this section, I discuss the flux budget related to the formed flux rope, manifested as the J-shaped bright feature, and the associated photospheric magnetic cancellation. Before the discussion about the flux budget in **Section 5.2**, I describe the magnetic configuration inferred in **Section 5.1**. As an additional finding, the conversion of the flux components after the J2 formation is described in **Section 5.3**.

5.1 Magnetic non-potentiality and magnetic configuration of sigmoid

At first, I discuss the magnetic configuration of J2. From **Section 4.2**, one of the footpoints of J2 has some signatures of magnetic non-potentiality (i.e., shear angles). The notable features exist in the region R1, R2, and R3, which are mentioned in **Section 4.2.3** and indicated in **Figure 4.7** (a1) and (a2). From these features I interpret the magnetic configuration as **Figure 5.1, 5.2**, and the left panel of **Figure 5.3**. As shown in these figures, the magnetic configuration of J2 should consist of the poloidal component, which is around the axis of flux rope, and the axial component, which is along the axis of flux rope as some previous studies (e.g. Bobra et al. 2008). The poloidal component should direct in left-handed around the axial component (see right panel of **Figure 5.2**), provided that sigmoid is inverse S-shaped (Titov & Démoulin 1999). The interpretations are summarized as follows.

1) The negative twist shear angle in other regions of the penumbra should be made by the sheared arcades near the PIL. The sheared arcades, manifested as filament threads appeared in 304 Å (see **Figure 4.10**), are related to the reconnection events observed in 131 Å (see **Figure 4.11**).
2) The positive twist shear angle in the region R2 should be made by the axial component of J2 along the inverse S-shaped sigmoidal feature (red arrow in the left panel of **Figure 5.2**).
3) The negative twist shear angle in the region R1, next to R2, should be made by the poloidal component of J2. Since the internal twist of J2 is left-handed, as mentioned above, the poloidal field underside of the axial field should form the positive shear in the penumbra near R2.
4) The negative dip shear angle in the region R3 should be made by the existence of J2, which connects to the higher layer of the atmosphere.

As mentioned above, dip shear angle and twist shear angle can be the physical parameters that enable us to extrapolate about the direction and time evolution of the internal field of MFRs and/or sheared arcades, although it is difficult to quantify the non-potentiality from shear angles.

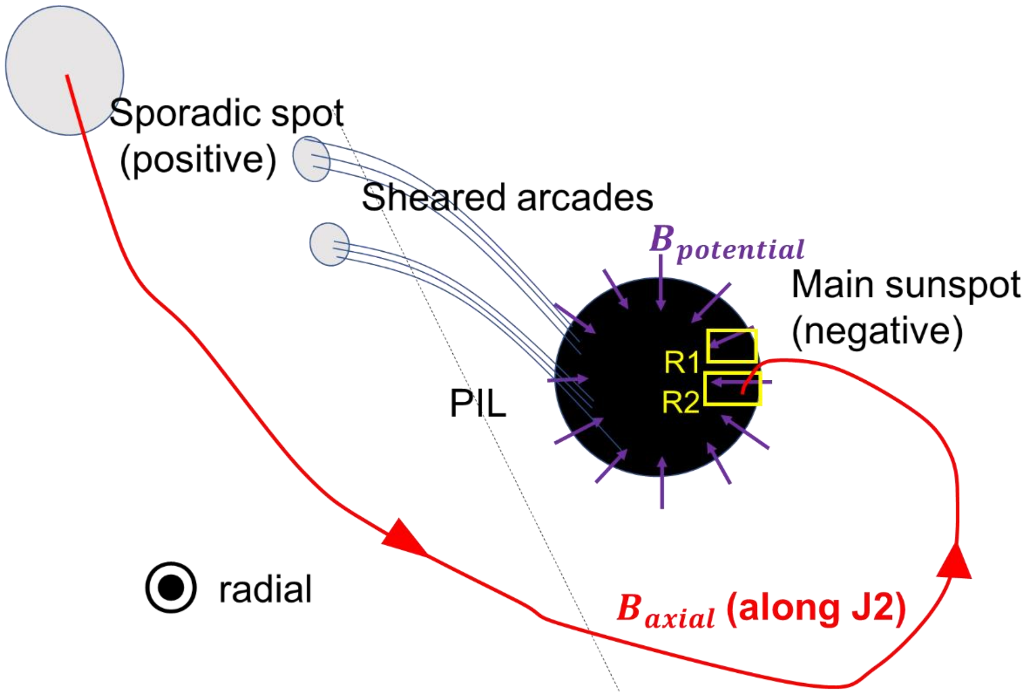

Figure 5.1

Schematic image of magnetic configuration of the whole AR 11692 seen in the vertically downward direction. The arrows indicate the horizontal components of vector magnetic field. $\boldsymbol{B}_{\boldsymbol{potential}}$ and $\boldsymbol{B}_{\boldsymbol{axial}}$ are the extrapolated potential field and the axial component respectively of magnetic field in J2. The yellow rectangles R1 and R2 are the regions of the extreme value of twist shear angle, described in **Section 4.2.3**.

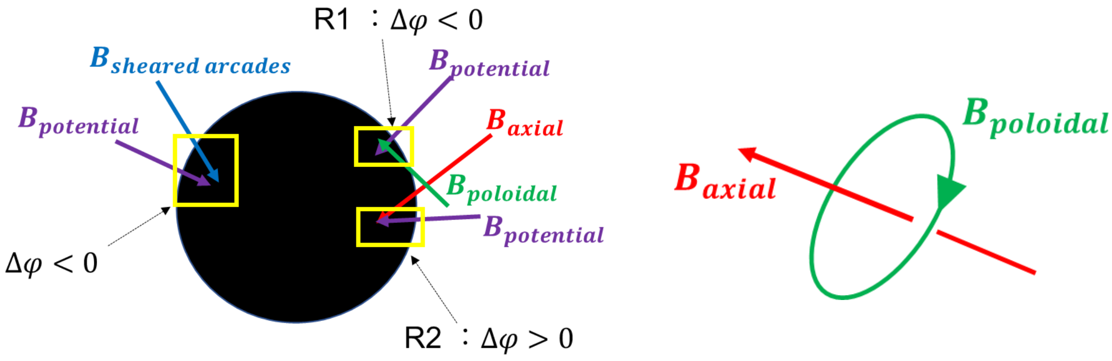

Figure 5.2

Left: Schematic image of magnetic configuration around the main sunspot of AR 11692 seen in the vertically downward direction. The arrows indicate the horizontal components of vector magnetic field. $\boldsymbol{B}_{potential}$, $\boldsymbol{B}_{axial}$, $\boldsymbol{B}_{poloidal}$, and $\boldsymbol{B}_{sheared\ arcades}$ are the extrapolated potential field, the axial component of magnetic field in J2, the poloidal component of magnetic field in J2, and the magnetic field in sheared arcades, respectively. The yellow rectangles are the regions of the extreme value of twist shear angle, described in **Section 4.2.3**. Right: The relation of the axial and poloidal components of magnetic field in flux rope J2.

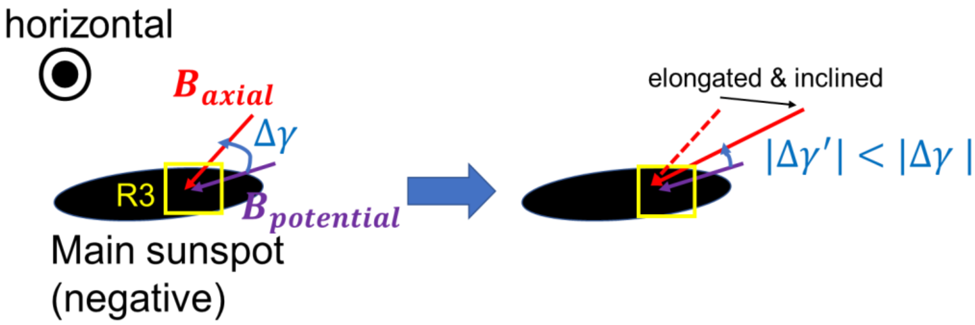

Figure 5.3

Schematic image of magnetic configuration around the main sunspot of AR 11692 seen in the horizontal northward direction. The arrows indicate vector magnetic field in a vertical plane. $\boldsymbol{B}_{\boldsymbol{potential}}$ and $\boldsymbol{B}_{\boldsymbol{axial}}$ are the extrapolated potential field, the axial component of magnetic field in J2 respectively. The yellow rectangle R3 is the region of the extreme value of dip shear angle, described in **Section 4.2.3**. The left and right images show the possible change of vectors and dip shear angle before and after the decrease of dip shear angle respectively.

5.2 Sigmoid formation and related changes of shear angles

Here I focus on the observed changes of shear angles and discuss them as signatures of the J2 formation. At first, the stream of the sigmoid formation can be separated to three terms; the first period (I) when the multiple reconnection events are occurred (before 17:35 UT on 14 March), the second period (II) from the final reconnection occurred to the J2 formation in a soft X-ray (from 17:35 to 21:30 UT on 14 March), and the third period (III) from the J2 formation to the onset of the flare (from 21:30 UT on 14 to 5:46 UT on 15 March).

5.2.1 dip shear angle

As shown in **Figure 5.4**, the average dip shear in R3 increases from negative value to zero, which means that the magnetic field gets more horizontal. I infer that this behavior results from the elongation of flux bundle J2, as shown in **Figure 5.3**. From **Figure 5.4**, we can see that this increase happened mainly after the multiple reconnection events, i.e., the periods (II) and (III). The J2 elongation should increase the poloidal flux if the poloidal flux per unit length along the axis of J2 is constant.

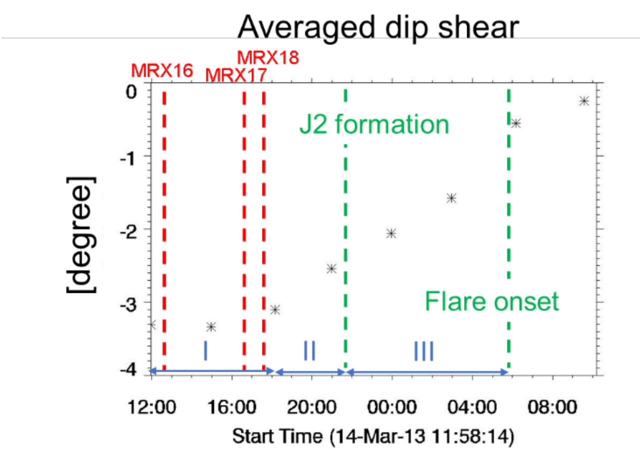

Figure 5.4

Time evolution of dip shear angle averaged in the region R3, which is the region of the extreme value of dip shear angle, described in **Section 4.2.3**. The red vertical broken lines represent the times of MRX16, MRX17, and MRX18. The green vertical broken lines represent the times of the J2 formation and the flare onset.

5.2.2 twist shear angle and flux budget

I interpret the changes of magnetic flux accumulated in the flux rope J2. As mentioned in **Section 5.1**, the regions R1 and R2 where twist shear angle is extreme value should correspond to the regions where poloidal and axial flux respectively in the footpoint of the flux rope J2. I summed flux in the regions where twist shear angle is less than -20, -15, and -10 degrees in the region R1 and the time evolution is shown in **Figure 5.5** (a). I also summed flux in the regions where twist shear angle is greater than 20, 15, and 10 degrees in the region R2 and the time evolution is shown in **Figure 5.5** (b). **Figure 5.5** (c) shows the time evolution of the summed flux in the region where the absolute value of twist shear angle is larger than 20, 15, and 10 degrees. It is noting that these thresholds 10, 15, and 20 degrees themselves have no physical meanings but enable me to extract the regions where twist shear is extreme. Here I assume that these values of summed flux correspond to the flux which J2 possesses.

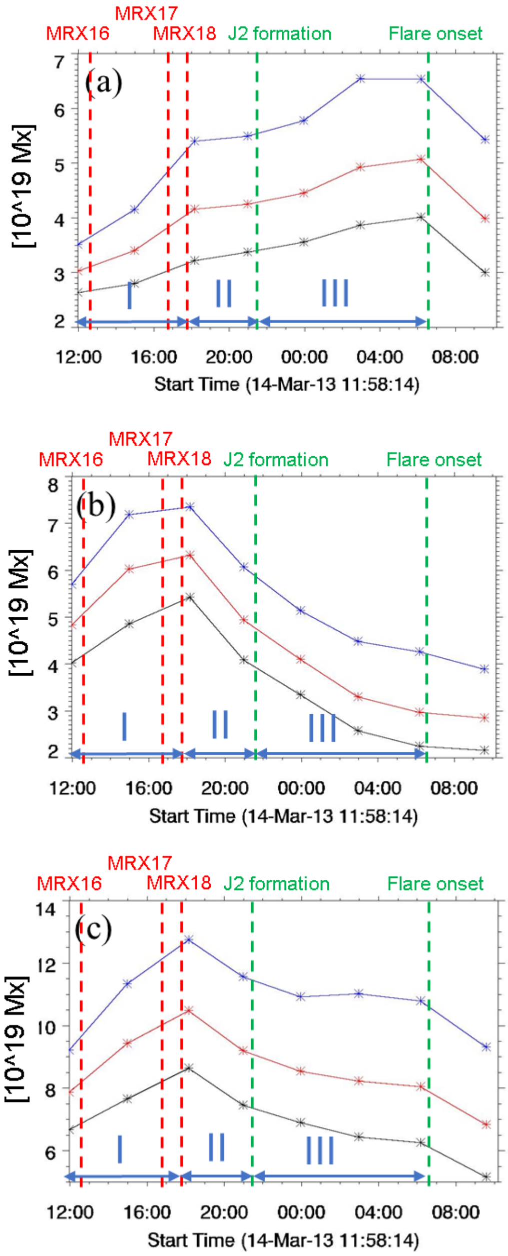

Figure 5.5 (a) Time evolution of the total flux in the region R1. The three curves represent the total flux in pixels where twist shear angle is less than -20 (black line), -15 (red line), and -10 degrees (blue line). **(b)** Time evolution of the total flux in the region R2. The three curves represent the total flux in pixels where twist shear angle is greater than 20 (black line), 15 (red line), 10 degrees (blue line). **(c)** Time evolution of the sum flux shown in the panels (a) and (b). The red vertical broken lines represent the times of MRX16, MRX17, and MRX18. The green vertical broken lines represent the times of the J2 formation and the flare onset.

From the red lines of **Figure 5.5**, in the period (I) poloidal and axial flux increase in 1.0 and 1.2 × 10^{19} Mx respectively. Thus, about 2.2 × 10^{19} Mx accumulated in the period. This fact is qualitatively consistent with the previously suggested model that flux cancellation drives flux to transfer to the flux rope. In this period, on the other hand, 0.85 × 10^{18} Mx is cancelled due to MRX15, MRX16, MRX17, and MRX18 with using **Table 4.1**. Therefore, in this period, around 4 % of the transferred to the flux rope is cancelled at the PIL. Savcheva et al. (2012) reported that NLFFF models for the 2007 February regions and the 2007 December region show that the sum of the poloidal and axial flux amounts to 60%–70% of the cancelled flux. This is consistent with the original flux cancellation idea if we think flux cancellation is the source of the flux in the flux rope and flux not participating in flux cancellation events is left as the arcade field. If the previous result is applied to this study, 2-3 % of the transferred to the flux rope is cancelled. From **Figure 4.4**, the total positive flux decreases in 8.0 × 10^{19} Mx. With using this value as the cancelled flux, it is shown that 27 % of the transferred to the flux rope is cancelled. This proportion, however, is also influenced by the reconnection between ambient field lines. In any case, this study produces different results from Savcheva et al. (2012) did; $\Phi_{cancelled} < \Phi_{flux\,rope}$ in the former and $\Phi_{cancelled} > \Phi_{flux\,rope}$ in the latter.

To reconcile the discrepancy, it should be noted that all the reconnected short field line cannot submerge toward under the photosphere. van Ballegooijen & Martens (1989) suggested that the submerging loop can pass the photospheric surface when the curvature force per unit volume at the top of the loop is larger than the buoyant force per unit volume. The former force is in inverse proportion to the local curvature radius R and the latter force is in inverse proportion to the pressure scale height H. The pressure scale height in the photosphere is lower than that in the subphotosphere because temperature in the former is lower than that in the latter. The photospheric surface, therefore, can act as the barrier for the submergence of the loop and the condition for the submergence can be written as $d < 2\pi H_{ph}$ ~ 900 km with the length of loop d and the photospheric pressure scale height H_{ph}. In AR 11692, the distance between the positive footpoint and the well-organized negative one is so long (longer than 1 Mm), which affects the comprehensively simple structure. On the other hand, AR 10977 and AR 11047, which are studied by Green et al. (2011) and Savcheva et al. (2012), are decayed bipolar active regions and the distances between positive and negative flux are shorter than that in AR 11692, thus the probabilities of the submergence in these active regions are higher.

In the period (II), only the axial flux seems to decrease (**Figure 5.5** (b)). This should be due to the elongation of the axis of the flux rope and the decrease of twist shear angle itself. As for the poloidal component, the increase of flux associated with the elongation, which is mentioned in **Section 5.1**, should make the decrease of flux small, although I cannot quantify the increase and the decrease individually because the axis of the flux rope in the period (II) cannot be observed in a soft X-ray and the length along the axis is not unclear.

Also, from **Table 4.1** the series of reconnection events contributes to the cancellation of flux of 7.69×10^{18} Mx, which is the total value of the cancelled flux associated with all the reconnection events. The sum of flux in the two regions is between ~ 7.4 and ~ 11×10^{19} Mx at the MRX18. These values indicate that 7 – 10 % of the flux rope is cancelled. This discrepancy may be because the potential-like arcade before the series of reconnection events already has flux participating in the following formed flux rope. From **Figure 5.5** (c), after J2 formation (period III) J2 possesses 6 - 12×10^{19} Mx. From **Figure 4.4**, the total flux is ~ 4.0×10^{20} Mx. These are almost consistent with the previous studies that the flux ropes have 20 – 50 % of the total flux in the active regions (Savcheva et al. 2012; Sterling et al. 2010).

5.3 Flux changes after J2 formation

From the J2 formation to the onset of the flare, the poloidal flux increased and the axial flux decreased in ~ 1 - 2×10^{19} Mx. This should be due to the conversion from axial flux to poloidal one. The ratio of the poloidal to axial is 0.7 – 0.9 when J2 is formed and becomes ~ 1.5 – 2 when the flare occurs. The behavior prior to the flare is qualititatively consistent with the kink instability (Torok et al. 2004). Previous studies had some efforts on the best-fit model for the inserted flux rope to be most closed to the observed magnetic configuration (Bobra et al. 2008; Su et al. 2009; Savcheva & van Ballegooijen 2009; Savcheva et al. 2012). They indicated that $\Phi_{pol} \ll \Phi_{axi}$ (Bobra et al. 2008; Su et al. 2009; Savcheva et al. 2012) or Φ_{pol} / Φ_{axi} ~1 / 4 (Savcheva & van Ballegooijen 2009) except for the time of the eruption. The ratio in this study is higher than those in these previous studies. This study indicate that a flux rope can exist constraining large amount of poloidal flux and the ratio Φ_{pol} / Φ_{axi} ~ 0.7 – 0.9. In the kinked flux rope model, a flux rope can be stable against the helical kink mode for a poloidal flux of up to Φ_{pol} / Φ_{axi} ~ 3 (Torok et al. 2004; Fan & Gibson 2004), thus the result of this observational study should make the ratio closer to the theories.

6. Conclusions and future prospects

6.1 Summary

The origin of solar flare has been identified as free magnetic energy accumulated in solar atmosphere. Sigmoid, which is a forward or inverse S-shaped bright feature appearing in soft X-ray, indicates sheared and / or twisted coronal magnetic structure (i.e. sheared arcade or magnetic flux rope) and likely to carry current and thus free magnetic energy. The formation processes of the magnetic structure have been shown as multiple magnetic reconnections in the atmosphere as well as flux emergence from the convective zone. The former process produces a longer helical field line and a shorter submerging one. When the submerging loop passes the photospheric surface, magnetic cancellation on the PIL is observed. The amount of the cancelled flux should be related to the internal flux of the sigmoidal magnetic structure.

In this thesis, I show the observational research about the relation between the formation of sigmoidal magnetic structure and the flux cancellation associated with magnetic reconnection in NOAA AR 11692. AR 11692 is the bipolar active region and has only a PIL and has little emerging flux, thus the active region is the most applicable as the target of the research about the contribution of only the cancellation event to the sigmoid formation. In two days prior to the formation of sigmoid in AR 11692, the coronal structure gradually evolves from a weakly sheared arcade to a J-shaped loop bundle, which is the southern part of the sigmoid.

The position of footpoint of the J-shaped bundle is identified with the estimation of twist and dip shear angle, which is the signature of non-potentiality in the photospheric level. I assume that the footpoint exists in the region where the absolute value of twist shear angle is extremely high and the sign of twist shear angle can separate poloidal and axial components in the flux rope.

I extracted the cancelled flux coupled with each of the magnetic reconnection events related to the J-shaped bundle and its total cancelled flux derived the total flux $\sim 7.69 \times 10^{18}$ Mx. I also estimated the accumulated flux in the J-bundle loop after its formation as the total value of flux in the regions near the footpoint as $7.4 - 11 \times 10^{19}$ Mx. Thus, the cancelled flux is 7-10 % of the flux in the flux rope. The magnitude correlation of the two values is inverse compared with the previous researches. This reflects lower probability of the submergence of the reconnected short loop due to longer distance between its two footpoints.

6.2 Future prospects

There are two aspects to be confirmed to improve this study. The first aspect is the relation between shear angles and magnetic configuration of flux rope. In a numerical simulation with flux insertion method (van Ballegooijen 2004), which is one of the NLFFF extrapolation methods and Savcheva et al. (2012) used for the flux estimation, poloidal flux per unit length and axial flux is parameters we can change. With fitting of these two parameters to the observed vector magnetic field, I can validate the flux estimation from magnetic shear angle. If this is validated, shear angles can be key factors at the point that only the observable magnetic field and potential field extrapolation let us estimate flux in flux ropes.

The second aspect is the dependence of the ratio of cancelled flux to flux in the flux rope on the distance between the two footpoints of the short loops. One of the specific features of AR 11692 is that the distance is long while the decayed active regions are investigated by the previous studies. I should investigate the contribution of the distance to the ratio from the statistical point of view.

Appendix1. Extraction of bright feature from soft X-ray images

Sigmoid can be identified as S-shaped or inverse S-shaped brighter structures than the surrounding structures in soft X-ray. I developed the identification method of sigmoid structures in soft X-ray images semi-automatically in collaborate with Iida, Y. and Kawabata, Y. The overall work flow of the identification is as follows.

a) Search enhancement ranges in frequency distribution of X-ray signal in each image.
b) Plot image of bright regions in each X-ray image by employing the lowest signals in each enhancement range found in a) as contour level.
c) Look for S-/J- shaped bright regions by eye and discriminate sigmoid structure when one or more S-/J-shaped regions can be found from 12 hours before the onset of the flare to the onset.

At first, we make frequency distribution of X-ray intensity in each image to determine noise level of XRT. All the data of XRT were normalized by the exposure time. The left panels in **Figure A1.1** show examples of the distribution at this step. There is a peak in the range smaller than 50 DN/s, which corresponds to the photon noise. We determine this value by fitting the distribution with Gaussian function for each image. The typical value of the noise is 15 DN/s.

Next, we look for enhancement in the frequency distribution. While the distribution typically falls as a power-law function in the range above the photon noise level, some enhancement ranges are occasionally seen. We extracted all such enhancements in the range larger than 100 DN/s, which is marked with triangles in the left column of **Figure A1.1**, as ranges where the first derivative of the frequency distribution is larger than 0. The middle column of **Figure A1.1** shows examples of this step. The horizontal line corresponds to 0 and the vertical dashed lines correspond to the lowest values of enhancement ranges discriminated in the analysis. Then, the bright enhancement region that is a candidate for sigmoid discrimination is drawn in an X-ray intensity image with the threshold value obtained in the above analysis. The right column of **Figure A1.1** shows the example of the enhancement regions found with this method. Colors of the contour lines correspond to those of the vertical dashed lines in the left and right columns.

At the final step of the sigmoid discrimination, we judge if the bright regions are S-or J-shaped. Iida, Y., Kawabata, Y., and I separately carried out this step with our eyes for all bright regions of all of the flare events whose photospheric magnetic field is measured by SOT/SP. When two or three persons judged that the bright region has a S- or J-shaped structure, the bright region is discriminated as a sigmoid. The flare event is judged to be accompanied with sigmoid when the sigmoidal structure exists at least one image from 12 hours before the flare peak time.

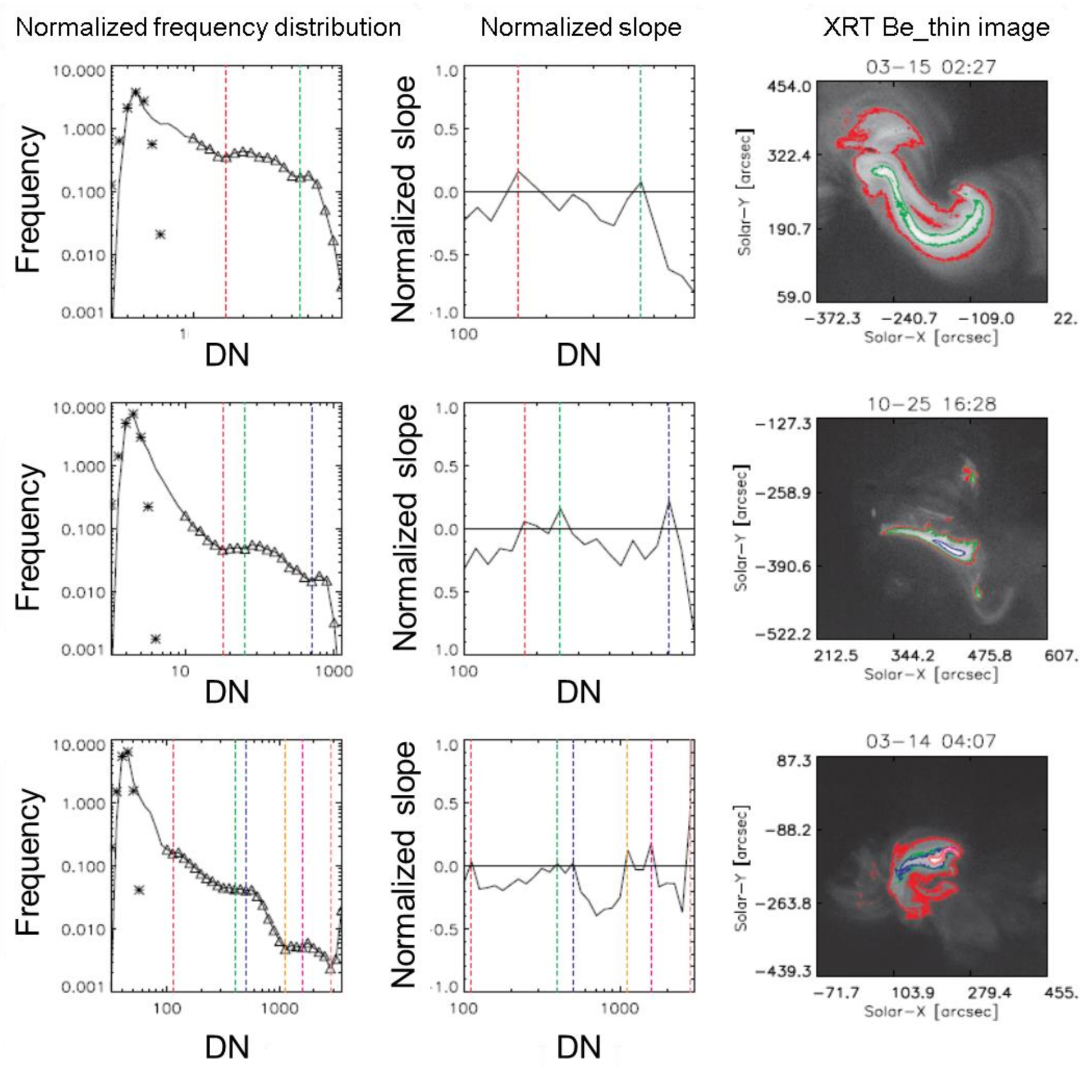

Figure A1.1 Examples of sigmoid structures in X-ray images. Left column shows frequency distribution of X-ray intensity in one image. The asterisks show fitting results by Gaussian function, which indicates photon noise in the image. The vertical dashed lines correspond to signals from which enhancement begins. Middle column shows derivative of frequency distribution of X-ray intensity. The horizontal line corresponds to 0 and the vertical lines correspond to the lowest signals of each enhancement range again. Right column shows the results of bright region detection. The background represents the X-ray intensity image and the contours show discriminated bright regions. The contour colors correspond to those in the left and middle columns.

Acknowledgements

This thesis is supported by many discussions with my supervisor, Prof. T. Shimizu. The members of my laboratory, Prof. T. Sakao, Dr. S. Ishikawa, Dr. D. Brooks, Dr. T. Kawate, Dr. Quintero, C. N., Dr. Y. Bamba, T. Oba, Y. Kawabata, T. Hasegawa, M. Abe, K. Daiguji, and Dr. T. Matsumoto encouraged and supported my research. The contents of this study are also contributed by helpful comments from Prof. T. Yokoyama, Dr. B. Kliem, and Dr. Y. Iida.

Hinode is a Japanese mission developed and launched by ISAS/JAXA, with NAOJ as domestic partner and NASA and STFC (UK) as international partners. It is operated by these agencies in co-operation with ESA and NSC (Norway). The SOT/SP level2 data are outputs from "inversions" using the HAO "MERLIN" inversion code developed under the Community Spectro-polarimetric Analysis Center (CSAC) initiative (http://www.csac.hao.ucar.edu/) at the National Center for Atmospheric Research, Boulder, Colorado, USA. *SDO* is the first mission to be launched for NASA's Living With a Star (LWS) Program, a program designed to understand the causes of solar variability and its impacts on Earth. This work was carried out by using *Hinode* Flare Catalogue (https://hinode.isee.nagoya-u.ac.jp/flare_catalogue/), which is maintained by ISAS/JAXA and Institute for Space-Earth Environmental Research (ISEE), Nagoya University. The data analyses were carried out on the system operated by the IT infrastructure managers of ISAS/JAXA and on the Solar Data Analysis System operated by the Astronomy Data Center of NAOJ.

Finally, I thank my family for supporting my life in this master course.

References

Antiochos, S. K., Dahlburg, R. B., & Klimchuk, J. A. 1994, Astrophys J, 420, 41

Antiochos, S. K., Macneice, P. J., Spicer, D. S., & Klimchuk, J. A. 1999, Astrophys J, 512, 985

Archontis, V., Hood, A. W., Savcheva, A., Golub, L., & Deluca, E. 2009, Astrophys J, 691, 1276

Aulanier, G., DeVore, C. R., & Antiochos, S. K. 2006, Astrophys J, 646, 1349

Baker, D., van Driel-Gesztelyi, L., & Green, L. M. 2012, Sol Phys, 276, 219

Bobra, M. G., Ballegooijen, A. A. Van, & Deluca, E. E. 2008, 1209

Canfield, R. C., Hudson, H. S., & McKenzie, D. E. 1999, Geophys Res Lett, 26, 627

Carmichael, H. 1964, Phys Sol Flares, 451

Chamberlin, P., Pesnell, W. D., & Thompson, B. 2012, Sol Dyn Obs, 9781461436, 1

Cheng, X., & Ding, M. 2016, Astrophys J Suppl Ser, 225, 16

Cheng, X., Ding, M. D., Zhang, J., et al. 2014

Fan, Y. 2001, Astrophys J, 554, L111

Gibson, S. E., Fan, Y., Mandrini, C., Fisher, G., & Demoulin, P. 2004, Astrophys J, 617, 600

Gibson, S. E., Fan, Y., Török, T., & Kliem, B. 2006, Space Sci Rev, 124, 131

Gibson, S. E., Fletcher, L., Del Zanna, G., et al. 2002, Astrophys J, 574, 1021

Golub, L., DeLuca, E., Austin, G., et al. 2007, Sol Phys, 243, 63

Gosain, S., & Venkatakrishnan, P. 2010, Astrophys J, 720, L137

Green, L. M., & Kliem, B. 2009, Astrophys J, 700, L83

Green, L. M., Kliem, B., Török, T., Van Driel-Gesztelyi, L., & Attrill, G. D. R. 2007, Sol Phys, 246, 365

Green, L. M., Kliem, B., & Wallace, A. J. 2011, Astron Astrophys, 526, A2

Hagino, M., & Sakurai, T. 2004, Publ Astron Soc Japan, 56, 831

Hirayama., T. 1973, Theor Model Flares Prominences, 1, 1689

Hudson, H. S., Lemen, J. R., St Cyr, O. C., Sterling, A. C., & Webb, D. F. 1998, Geophys Res Lett, 25, 2481

Ishii, T. T., Kurokawa, H., & Takeuchi, T. T. 1998, Astrophys J, 499, 898

Kano, R., Sakao, T., Narukage, N., et al. 2008, Publ Astron Soc Japan, 60, 827

Kliem, B., Titov, V. S., & Torok, T. 2004, Astron Astrophys, 413, L23

Kopp, R. A., & Pneumann, G. W. 1976, Sol Phys, 50, 85

Kosugi, T., Matsuzaki, K., Sakao, T., et al. 2007, Sol Phys, 243, 3

Kumar, P., Yurchyshyn, V., Cho, K. S., & Wang, H. 2017, 36, 1

Kumar, P., Yurchyshyn, V., Wang, H., & Cho, K. S. 2015, Astrophys J, 809 (IOP Publishing), 83

Kurokawa, H., Wang, T., & Ishii, T. T. 2002, Astrophys J, 572, 598

Lemen, J. R., Title, A. M., Akin, D. J., Boerner, P. F., Chou, C., Drake, J. F., Duncan, D. W., Edwards, C. G., Friedlaender, F. M., Heyman, G. F., Hurlburt, N. E., Katz, N. L., Kushner, G. D., Levay, M., & Russ, N. W. 2012, Sol Phys, 275, 17

Li, T., & Zhang, J. 2015, Sol Phys, 290, 2857

Lin, J., & Forbes, T. G. 2000, J Geophys Res Sp Phys, 105, 2375

Lites, B. W. 2005, Astrophys J, 622, 1275

Lites, B. W., Elmore, D. F., K. V. S. 2007, ASP Conf Ser, 369

Mackay, D. H., Karpen, J. T., Ballester, J. L., Schmieder, B., & Aulanier, G. 2010, Space Sci Rev, 151, 333

Martin, S. F. 1998, 107

Martin, S., Livi, S., & Wang, J. 1985, Aust J Phys, 38, 929

Mckenzie, D. E., & Canfield, R. C. 2008, 68, 65

Metcalf, T. R., Leka, K. D., Barnes, G., et al. 2006, Sol Phys, 237, 267

Okamoto, T. J., Tsuneta, S., Lites, B. W., et al. 2008, Astrophys J, 673, L215

Okamoto, T. J., Tsuneta, S., Lites, B. W., et al. 2009, Astrophys J, 697, 913

Poisson, M., López Fuentes, M., Mandrini, C. H., Démoulin, P., & Pariat, E. 2013, Adv Sp Res, 51, 1834

Rust, D. M., & Kumar, A. 1996, Astrophys J, 464, L199

Savcheva, A. S., Green, L. M., van Ballegooijen, A. A., & DeLuca, E. E. 2012, Astrophys J, 759, 105

Schmieder, B., Aulanier, G., & Vršnak, B. 2015, Sol Phys, 290 (Springer Science+Business Media Dordrecht), 3457

Schou, J., Scherrer, P. H., Bush, R. I., et al. 2012, Design and ground calibration of the Helioseismic and Magnetic Imager (HMI) instrument on the Solar Dynamics Observatory (SDO), The Solar Dynamics Observatory, Vol. 9781461436

Shibata, K., & Magara, T. 2011, Living Rev Sol Phys, 8, 6

Shibata, K., Masuda, S., Shimojo, M., et al. 1995, Astrophys J, 451, 83

Shimizu, T., Katsukawa, Y., Matsuzaki, K., et al. 2007, Publ Astron Soc Japan, 59, 845

Shimizu, T., Nagata, S., Tsuneta, S., et al. 2008, Sol Phys, 249, 221

Sterling, A. C., & Hudson, H. S. 1997, Astrophys J, 491, L55

Sterling, A. C., Chifor, C., Mason, H. E., Moore, R. L., & Young, P. R. 2010, Astron Astrophys, 521, A49

Sturrock, P. A., & Coppi, B. 1966, Astrophys J, 143, 3

Suematsu, Y., Tsuneta, S., Ichimoto, K., et al. 2008, Sol Phys, 249, 197

Titov, V. S., & Démoulin, P. 1999, Astron Astrophys, 351, 707

Tripathi, D., Kliem, B., Mason, H. E., Young, P. R., & Green, L. M. 2009, Astrophys J, 698, L27

Torok, T., Kliem, B., & Titov, V. S. 2004, A&A, 413, L27

Tsuneta, S., Ichimoto, K., Katsukawa, Y., et al. 2008, Sol Phys, 249, 167

van Ballegooijen, A. A., & Martens, P. C. H. 1989, Astrophys J, 343, 971

van Ballegooijen, A. A. 2004, Astrophys J, 612, 519

Vourlidas, A., Lynch, B. J., Howard, R. A., & Li, Y. 2013, Sol Phys, 284, 179

Wang, H., Cao, W., Liu, C., et al. 2015, Nat Commun, 6 (Nature Publishing Group), 1

Yokoyama, T., Shibata, K. 1995, Lett to Nat, 375, 42

Zirin, H., & Liggett, M. A. 1987, Sol Phys, 113, 267